
Article:
Kahavita, K.D.H.N., McCarthy, E.D., Zhang, M. et al. (2026) Characterising the shear, stretch and in-plane bending response of a pure-unidirectional non-crimp fabric. International Journal of Material Forming, 19 (1). 14. ISSN: 1960-6206

https://doi.org/10.1007/s12289-026-01978-z

International Journal of Material Forming (2026) 19:14
https://doi.org/10.1007/s12289-026-01978-z

RESEARCH

Characterising the shear, stretch and in-plane bending response of a pure-unidirectional non-crimp fabric

K. D. H. N. Kahavita[1] · E. D. McCarthy[2] · M. Zhang[3] · C. M. Ó Brádaigh[4] · P. Harrison[1]

Received: 15 August 2025 / Accepted: 6 January 2026

Abstract
The in-plane deformation kinematics of a pure-Unidirectional Non-Crimp Fabric (pure-UDNCF) is investigated using novel and existing experimental methods to characterise its shear, tensile, and in-plane bending responses under controlled loading. A pure-UDNCF is defined as a fabric in which stabilising tows are absent in the transverse direction relative to the primary tow orientation. The stitching threads in this fabric are made of polyamide, a highly compliant material that allows significant stretch, introducing a low-energy deformation mode that is relatively absent in biaxial engineering fabrics and quasi-UDNCFs (UDNCFs with inextensible stitching and transverse stabilising fibres). To fully characterise its forming behaviour, several novel testing methods are introduced that generate well-defined combinations of fabric shear, in-plane bending and stitch tensile strain. The total normalised axial force measured in the tests is subsequently decoupled into three contributions from shear, tensile strain in the stitch direction, and in-plane bending of the tows. An important finding is that when tested in the picture frame test, in-plane bending generates more resistance to specimen deformation than shearing of the fabric. The testing protocol and resulting data can be used to create appropriate constitutive models for pure-UDNCFs.

Keywords Unidirectional stitched non-crimp glass fabric · Uniaxial bias extension test · In-plane shear · Strain in stitch direction · In-plane bending

Introduction

Composites reinforced with synthetic fibres such as glass, carbon and aramid are under increasing demand in aerospace, automotive and structural engineering industries as substitutes for conventional materials like metals due to their unique advantages such as high specific stiffness, strength, energy absorption capacity, and lightweight, together with good chemical and corrosion resistance [1, 2]. Depending on how the fibres are oriented within the textile, the yarn arrangement can be categorised as straight (non-crimp), low undulation (woven and braided), or looped (knitted) [3]. Non-crimp fabrics (NCF) are popular in demanding structural applications because laminates manufactured with NCFs exhibit higher compressive and tensile mechanical properties than 2D woven fabric composites due to lower waviness (out-of-plane undulation) [4, 5]. In addition, NCFs are generally stable during handling due to the presence of stitching that holds the fibres in place. The stitching prevents fibre movement and maintains the intended fibre orientation, minimising the risk of unwanted deformation or misalignment [6, 7].

In comparison to the extensive research conducted on biaxial NCFs [6, 8–10], there has been relatively limited investigation into the experimental and numerical analysis of dry unidirectional NCFs (UDNCFs), which are used in preforming processes before resin infusion. Previous UDNCF investigations have mostly focused on quasi-UDNCF; these contain a small weight fraction of glass fibre

✉ P. Harrison
Philip.Harrison@glasgow.ac.uk

1 James Watt School of Engineering, University of Glasgow, Glasgow G12 8QQ, UK

2 The School of Engineering, Institute for Materials and Processes, The University of Edinburgh, Edinburgh EH9 3FB, UK

3 Johns Manville, Denver, CO, USA

4 Faculty of Engineering, The University of Sheffield, Sir Frederick Mappin Building, Mappin Street, Sheffield S1 3JD, UK

Published online: 11 February 2026

tows oriented transverse to the main tow direction to stabilise the fabric during forming [11–14] and relatively little work has focused on understanding the forming behaviour of UD fabrics containing no transverse stabilising tows and with extensible stitching [15–17], referred to here as pure-UDNCFs. The use of compliant stitching radically changes the deformation mechanics of the fabric by providing an alternative mode of deformation during forming; the fabric can both shear and extend in the stitch direction during forming. This effectively makes these fabrics more formable and less prone to wrinkling during complex forming operations than most other NCFs, though. On the downside, the use of polymeric stitching can lead to fabric distortion when subjected to temperature changes, and excessive extension in the stitch direction during forming can result in the opening of gaps and holes in the fabric [18]. Furthermore, when polyamide stitching is used, its hydrophilic nature may contribute to moisture uptake, which can affect resin infusion quality and potentially reduce the long-term durability of the composite.

Characterising the forming behaviour of pure-UDNCFs presents a challenge. Typically, the Picture Frame (PF) and Uniaxial Bias Extension (UBE) tests are used to characterise the shear behaviour of engineering fabrics. Some researchers performed off-axis-tension experiments with fibre angles of 30˚ and 60˚ in addition to 45˚ (bias extension) to determine different ratios of in-plane shear and tensile strains of quasi-UDNCFs [19–21]. The results suggest that the 45˚ off-axis test is best suited to characterise the shear deformation of quasi-UDNCFs because it aligns the loading direction with the principal shear direction, maximising the shear strain component while minimising axial effects. A recent investigation, comparing PF and UBE test results on the same pure-UDNCF, showed a significant reduction in the measured shear stiffness of the fabric plotted against shear angle when measured in the UBE test compared to the PF test [15]. In that investigation, a possible explanation for the lower measured force in the UBE test was that the observed extension in the stitch direction during the UBE test significantly reduced the fabric's shear resistance. However, some doubt around that conclusion remained, and although standard UBE and PF tests provide important insights into the forming behaviour of pure-UDNCFs, their results alone were thought to be insufficient to fully characterise the forming mechanics of pure-UDNCFs. Consequently, the development of novel experimental methods to better understand the fundamental mechanical forming properties of pure-UDNCF is required. This investigation presents alternative new test methods in response to this problem. By creating tests with well-defined kinematics, combining different amounts of fabric shear, stretching along the stitch direction, in-plane bending and transverse compression of the tows, the effect of these kinematics on the measured axial force can be explored. Each test used in this investigation accesses different regions of the (shear angle) – (tensile stretching) parameter space and, as will become apparent, some tests induce in-plane bending of the tows and/or transverse compression of the tows, while others do not. To effectively model the forming behaviour of the pure-UDNCF, it is necessary to separate the contributions to the measured axial force from shear, stitch tension and in-plane bending. The aim is to demonstrate a characterisation protocol for this unusual type of fabric. The work is also of relevance to researchers incorporating in-plane bending and second-order gradient kinematics into constitutive models for unidirectional composites [22] and engineering fabrics, e.g. Cuomo et al. [23] and Bai et al. [24]. The effect of in-plane bending stiffness has been observed to affect testing, not just on pure-UDNCFs but also on UD prepregs, e.g. McGuinness and ÓBrádaigh [25]. Its inclusion in forming models has been shown to improve predictions of fibre direction and wrinkle generation in complex forming simulations [26, 27]. Nevertheless, direct measurement of in-plane bending stiffness remains challenging and is usually inferred via inverse modelling of kinematics [26–28]. A contribution of this work is therefore to provide a method of experimentally measuring and isolating the in-plane bending stiffness of pure-UDNCFs.

The structure of the remainder of the paper is as follows. The section *'Material'* describes the fabric and briefly summarises the potential deformation kinematics of the fabric. The first part of the *'Experimental Methods'* section focuses on *'Standard Test Methods'*, the second part outlines *'Novel Test Methods'*. Both parts briefly review the methods and their associated kinematic equations. A video showing each of the test methods is available (see Video 1). In the *'Results'* section, data are reported first in terms of the measured specimen kinematics and then in terms of measured forces (initially plotted in 2D, then in 3D parameter space). The section, *'Isolating the Contributions'* is dedicated to interpreting the results. Here, the aim is to isolate the contributions to the measured force from shear, stitch stretching and in-plane bending. Finally, key findings are summarised in the *'Conclusions'* section.

Material

A unidirectional tricot-chain stitched non-crimp glass fabric (supplied by Johns Manville) with an areal density of 1370 ± 14 g/m^2 is investigated (see Fig. 1). A tricot-stitch (67 dtex) runs across the back of the fabric along the glass tows (Johns Manville StarRov® 886–2400 tex), while a chain-stitch runs across the front in the weft direction. This

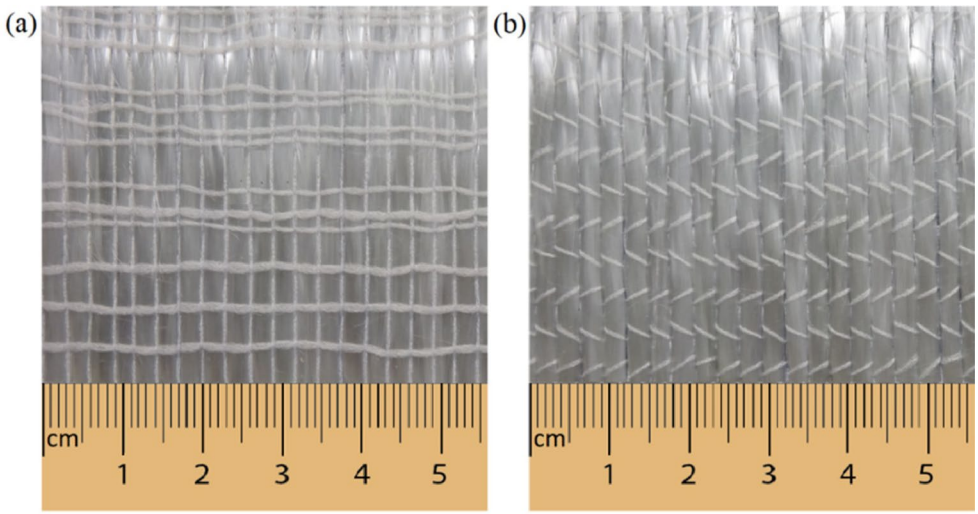

Fig. 1 Image of unidirectional non-crimp glass fabric surface with tricot-chain stitching pattern (**a**) front (**b**) back. Bottom scale increments are in cm

polyamide stitch architecture means that in the initial undeformed state, the tows and chain stitch are perpendicular to each other, resulting in symmetric shear behaviour of the NCF [29]. The average widths of the tows and stitches were measured using ImageJ [30] to be 2.6 ± 0.5 mm and 0.6 ± 0.1 mm, respectively (the error represents +/- 1 standard deviation from 10 measurements). Figure 2 shows the various deformations that could potentially occur in the fabric. This investigation focuses on relatively easy-to-measure macro-strains and not on meso-scale deformation mechanisms such as slip (lower row of images), though no evidence of the latter was observed in these tests.

Experimental methods

This section is divided into two parts. The first briefly describes three standard engineering fabric testing methods used in this investigation (tensile, picture frame and uniaxial bias extension tests), while the second explains three novel test methods (cruciform bias extension, parallelogram shear-stretch and simple shear tests) developed specifically to better characterise the mechanical forming behaviour of the pure-UDNCFs under study. All tests described in this paper were conducted using a Zwick Z2 electromechanical test machine with a 2kN loadcell. Four repeats of each test

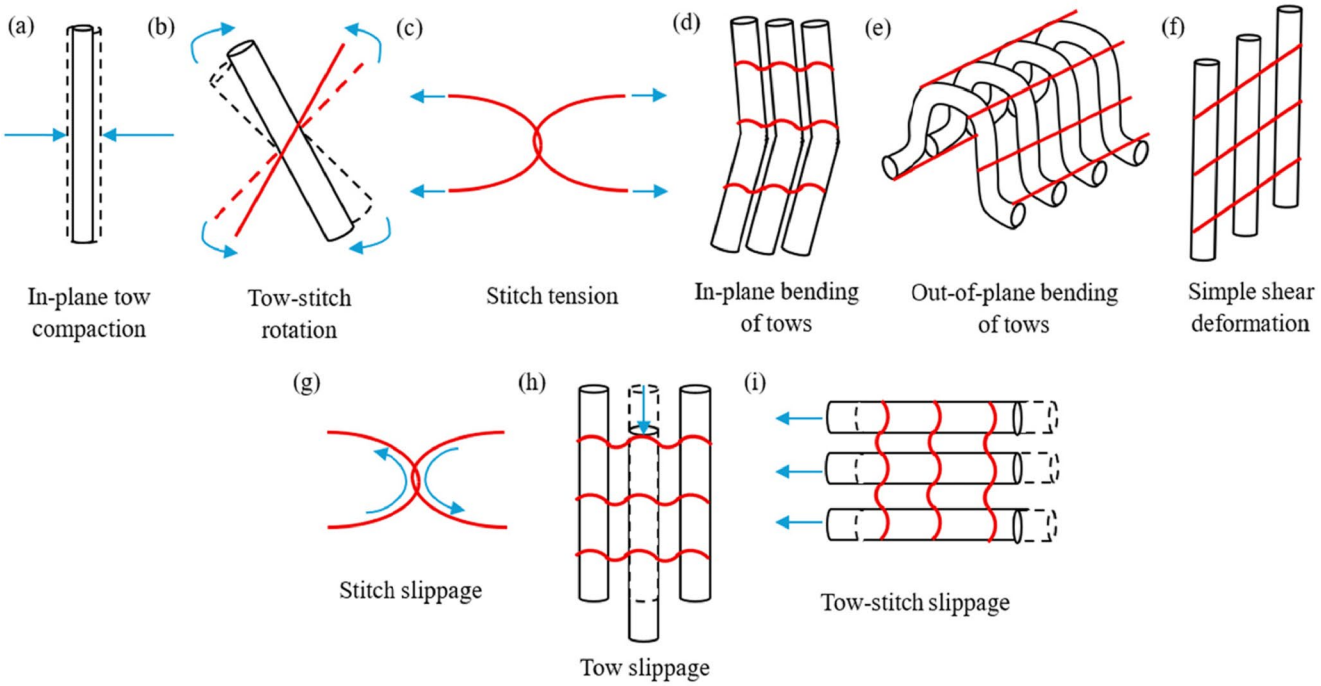

Fig. 2 Potential deformation modes of Pure-UDNCF

were performed, except for the Cruciform Bias Extension (CBE) test. The front face of the test specimen was recorded with a Casio EX-ZR700 digital camera. Manual image processing was performed using ImageJ [30] to measure the specimen kinematics, including the shear angle and stretch in the stitch direction. In contrast to quasi-UDNCF, the lack of stabilising fibres may cause early stretching in the stitch direction when handling the pure-UDNCF. This can cause significant variation in the outcome of each test, similar to the pre-shear angle error of the UBE test discussed in [31]. To determine the pre-stretching in the stitch direction of the specimens, it is necessary to define the number of tows per unit length for the undeformed material. The initial state of the fabric was considered to be the condition after the fabric was cut from the roll and relaxed on a flat surface. The number of tows per 50 mm width of fabric was measured. Depending on the tow width, the number of tows per 50 mm varied from 16 to 18 and the average value of 17 tows per 50 mm stitch length was selected as the standard tow count in the initial state of the fabric. In each test, adjustments to account for unintended pre-stretch error were made (see [32] for details).

Standard test methods

Three standard tests have been used in this investigation: the Tensile, Picture Frame and Uniaxial Bias Extension tests.

Tensile test

A tensile test was performed on pure-UDNCF in accordance with the ISO 13934-1. Specimens with an initial length along the stitch direction, L_T, of 50 mm and an initial width, W_T, of 200 mm were prepared to test the tensile properties of the pure-UDNCF in the stitch direction at a strain rate of 20 mm/min (see Fig. 3). The engineering strain in the stitch direction during the tensile test, ϵ_T, is calculated as a function of the displacement, D_T (see Eq. 1).

$$\epsilon_T = \frac{D_T}{L_T} \tag{1}$$

Uniaxial bias extension and modified picture frame tests

The shear behaviour of the pure-UDNCF was investigated using both standard UBE and modified PF tests. The standard UBE test is well-documented and is typically used to characterise biaxial fabrics with (practically) inextensible tows (typically less than 1–2% strain under forming loads) [33, 34]. For biaxial fabrics, the UBE specimen can be divided into three areas, namely, Regions A, B and C (see Fig. 4a). If no inter-tow slip (where inter-tow slip refers to the sliding of tows relative to each other at their crossover points, distinct from the natural rotation of tows during fabric shear deformation) occurs throughout the test, then the shear angle of Region B will be half that of Region A [14]. The UBE setup suggested in [33] involves bonding aluminium foil on both sides of Region C using epoxy resin. As a result, Region C remains undeformed, mitigating intra-ply slip and any associated energy contributions from this region.

When considering shear deformation in Region A (see Fig. 4b), the initial inter-fibre angle, $\phi_{s(i)}$ is 90° if the warp and weft tows in the specimen are perpendicular to one another. The change in the inter-fibre angle, ϕ_s, can be determined by the dimensional change of Region A (see Fig. 4b). If the aspect ratio of the specimen, λ ($\lambda = H/W$, where H and W are the height and width of the specimen, respectively, see Fig. 4a), are greater than 2 [34], the extended length, d_s, can be predicted as,

$$d_s = 2\,(\lambda - 1)\,L_A \left[\cos\left(\frac{\phi_s}{2}\right) - \cos\left(\frac{\phi_{s(i)}}{2}\right)\right] \tag{2}$$

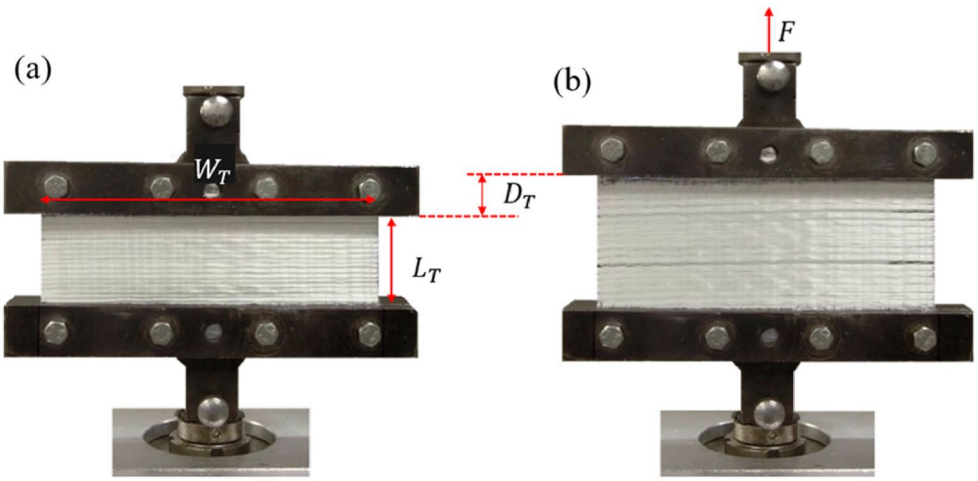

Fig. 3 Tensile test specimen (**a**) undeformed (**b**) deformed

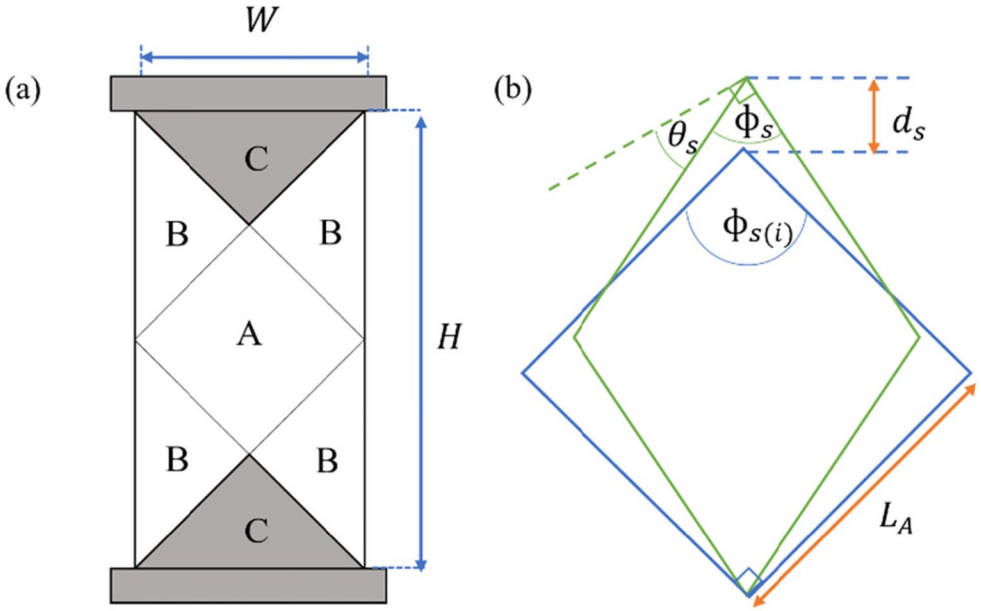

Fig. 4 (**a**) An undeformed UBE specimen (**b**) Shear deformation in Region A

where, L_A is the initial side length of Region A. The inter-fibre angle at a given displacement, ϕ_s, can be calculated by rearranging Eq. (2) as,

$$\phi_s = 2\ acos\left[\frac{d_s}{2\,(\lambda\ -1)\,L_A} + \cos\left(\frac{\phi_{s(i)}}{2}\right)\right] \tag{3}$$

The shear angle, θ_s, can then be determined by the difference between the initial inter-fibre angle ($\phi_{s(i)}$ = 90°) and inter-fibre angle at a given displacement, ϕ_s.

$$\theta_s = \frac{\pi}{2} - 2\ acos\left[\frac{d_s}{2\,(\lambda\ -1)\,L_A} + \cos\left(\frac{\phi_{s(i)}}{2}\right)\right] \tag{4}$$

In the UBE test, two of the four sides of the specimen are clamped orthogonal to the bias direction (see Fig. 5a). The clamping of the tows is only at one end, leaving the other end free. Because the stitches have only a small tensile stiffness, tensile stretching of the pure-UDNCF in the stitch direction is possible. The deformation of the UBE specimen will, therefore, 'choose' the path resulting in minimum energy. The less constrained UBE test results in significantly different kinematics than the PF test. This can be observed by monitoring the side lengths of Region A, L_A and L'_A in the UBE test (see Fig. 5a&c). This is approximately equal on either side of Region A at the beginning of the UBE test (see Fig. 5a); however, it increases along the stitch direction (L'_A - see Fig. 5c) during the test. Furthermore, the blue line drawn in the PF specimen remains horizontal during the test (compare Fig. 5b&d), whereas the line becomes oblique in the UBE test (compare Fig. 5a&c) due to stretching in the stitch direction. Schirmaier et al. [12], Ghazimoradi et al. [13], and Schäfer [21] focused on quasi-UDNCFs, which contain a small weight fraction of stabilising fibres in the direction initially transverse to the main fibres. They reported similar kinematics, but the stretching of their NCFs in the stitch direction was much lower compared to the pure-UDNCF used in the current work. By comparing ideal 'pure' shear and 'simple' shear, the degree to which type of behaviour the fabric follows can be ascertained (see Eqs. (2) & (12) in Pourtier et al. [35] for pure and simple shear, respectively), i.e., the influence of stretching in the stitch direction for pure-UDNCFs, or the amount of inter-ply fibre slip for biaxial and quasi-UDNCFs. The equation describing simple shear kinematics, derived by Pourtier et al. [35], is used later in this investigation. Equation 5 presents the theoretical shear angle, γ, derived in [35] (see Eq. (12) in [35]) for simple shear deformation, consistent with the symbols used in Fig. 4 of this study.

$$\gamma\ (d_s) = \frac{\pi}{2} - sin^{-1}\ (K) - sin^{-1}\left(\frac{L_A.\,K}{L_A^2\,K^2 + \sqrt{(d_s + \sqrt{2}\,L_A - L_A\sqrt{1-K^2})^2}}\right) \tag{5}$$

$$\text{with } K = \frac{\sqrt{2}}{2}\left(\frac{1}{1+\left(\frac{d_s}{H-W}\right)}\right)$$

A rectangular-shaped specimen of 400 × 200 mm was selected for this study, and [36] describes all the steps of the UBE sample preparation in detail. Note that no out-of-plane wrinkling was generated during these UBE tests in Region A (the use of anti-wrinkle plates [37] was unnecessary). One observation noted in the UBE test on pure-UDNCFs was that the kinematics in Regions B of the UBE specimen were not uniform (marked as B1 and B2, see Fig. 5a). In the B1

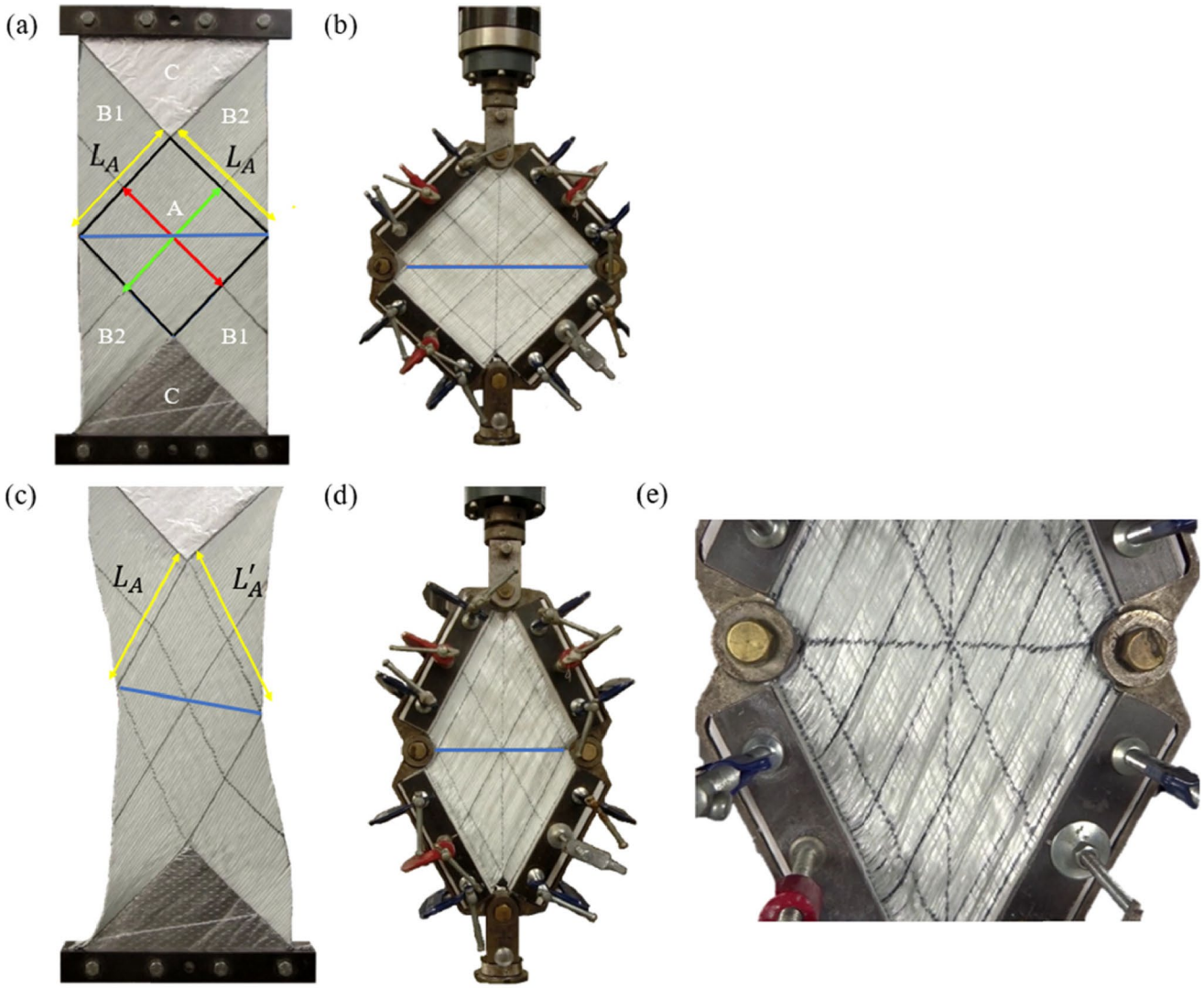

Fig. 5 (**a**) Undeformed UBE test specimen ($400 \times 200 mm^2$), the red and green arrows indicate the initial chain-stitch direction and the tow direction, respectively (**b**) undeformed PF test specimen ($170 \times 170 mm^2$) (**c**) UBE test specimens at a shear angle of 35° (**d**) PF test specimens at a shear angle of 35°. The blue line connects the lateral corners of the specimen's central region; it is a useful direction to track during the shear tests. (**e**) Close-up of the same test showing in-plane bending near the bottom-left clamp

Regions, one end of the tows is constrained, and both ends of the stitches are unconstrained whereas in the B2 Regions, one end of the stitches is constrained, and both ends of the tows are unconstrained. These complex dynamics limit the development of a theoretical analysis of the test kinematics. Consequently, an alternative, more constrained version of the standard UBE test was developed (see Section on *'Novel Test Methods'*). Another important point to observe in Fig. 5c is that in-plane bending of the tows is almost entirely absent during shear of the fabric in the UBE specimens.

A modified PF test method, involving the use of G-clamps applying both low and high clamping pressure, was demonstrated to eliminate most of the error due to misalignment. See [15] for a fully detailed description of the setup and sample preparation of the PF test. The PF rig consists of four bars connected to each other by rotating hinges fitted with bearings (see Fig. 5b). A source of friction in the PF test can come from the bearings or the mating surfaces of the four arms of the rig (i.e., the contact interfaces between adjacent arms of the rig within the hinge assemblies, resulting in resistance to frame-arm rotation). This friction can potentially lead to overestimation of the mechanical stiffness of the fabric. Further, adding extra weights in the form of G-clamps (see modifications of the PF test discussed in [15]) can increase the rig's mass and consequently the frictional forces measured during the test. A series of friction tests was therefore performed to quantify friction in the rig and then isolate the actual fabric shear response based on those results. Note that, prior to conducting the tests reported in [15], the rig appeared to have no significant friction when pulled by hand, and a test to measure the friction of

the unloaded PF rig suggested very little resistance (approximately 1 N/m or 0.17 N). A full account of how the PF results have been modified to account for rig friction is provided in [32]. The results suggested that the rig-friction does indeed make a small contribution to the axial force, especially if the load on the rig is increased (e.g. by using G-clamps, see Fig. 5b). This experience suggests that conducting a friction measurement test on the rig prior to testing a fabric, even though the rig may appear frictionless when manually tested by hand, is recommended. All force results from the PF test reported in this investigation (see *'Results'* section) have been modified to account for friction in the PF rig.

The theoretical shear angle for the PF tests of this investigation was calculated using Eq. (1) in Kahavita et al. [15]. Finally, it is important to note that, even when using G-clamps rather than fully clamping the specimen [15], in-plane bending of the tows in the PF specimen still occurs next to the PF rig clamps, resulting in meso-scale buckling of the tows emerging from beneath the clamps, see Fig. 5e. This is a well-documented effect for the PF test. According to Willems et al. [38], the local bending phenomenon occurs along the edges of the frame, and this bending is particularly noticeable in the parts of the arm that are considered 'stiff' (see Fig. 5c in [38]). This phenomenon was further investigated by Krogh et al. [39] on satin-woven carbon-fibre prepreg samples with three different PF arm geometries, i.e., full arms, arms with cutting slits, and arms in which the transverse tows were removed. S-shaped deformation is clearly observed in samples without transverse tows (see Fig. 8 in [39]), and as the shear angle increases, the in-plane bending effect increases.

Development of novel test methods

This section describes several novel test methods, each designed to induce well-defined forming kinematics and explore different regions of shear-stretch parameter space, not accessible using the standard test methods.

Cruciform Bias Extension (CBE) test

In this experiment, the shape of the regular UBE specimen was modified to an octagonal shape. Aluminium foil was bonded to all four C Regions of the specimen (see Fig. 6a), which effectively removed any significant contribution to the measured axial force from the deformation of Region C and helped to generate a well-defined strain field across the specimen. Consequently, the actively deforming region of the specimen was initially of a cruciform shape (see Fig. 6a, referred to here as the CBE test). One goal was to create better-defined kinematics across the whole specimen compared to the UBE test, and another was to produce a different combination of shear and tensile strain in the stitch direction, compared to the UBE test, and thereby allow measurements to be performed across a different region of the (shear angle) – (tensile stretching) parameter space. Alternative bias-extension test geometries have been used previously by various researchers, including Harrison et al. [40] and Krogh et al. [11].

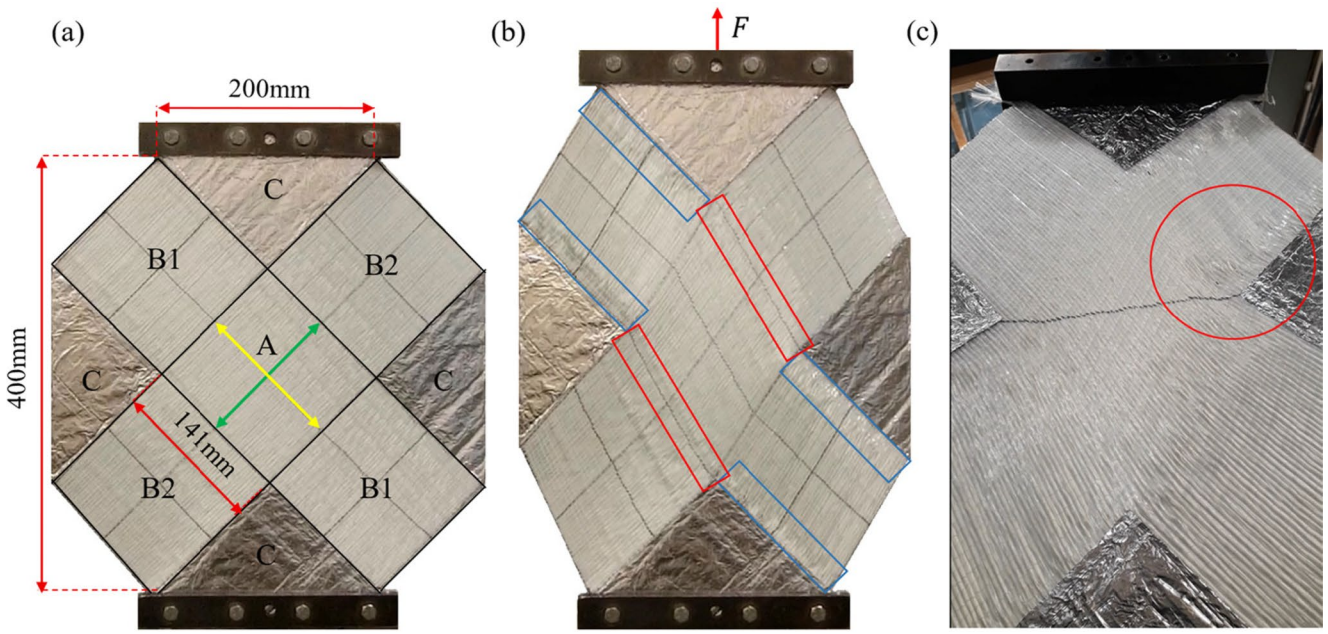

Fig. 6 CBE specimen (**a**) undeformed. The yellow and green arrows indicate the initial chain-stitch and tow directions, respectively. (**b**) deformed at a shear angle of 30°, marked areas highlight in-plane bending of tows (red – high, blue – low) (**c**) wrinkle onset, the area circled in red indicates the formation of wrinkles in the B1 Region

As with the UBE kinematics for pure-UDNCF (see Fig. 4a), the octagonal-shaped shear specimen can also be divided into four regions, namely, A, B1, B2 and C. Note that, as for the UBE test, Eqs. (2–4), with $\lambda = 2$, would describe the kinematics of the CBE specimen, if it were conducted using a biaxial fabric following pin-jointed net kinematics [40]. As with the UBE test results, a comparison of the measured kinematics with the predictions for both pure (Eq. 4) and simple shear (Eq. 5) provides insight into the measured kinematics (see '*Kinematics'* section). Note that out-of-plane wrinkling was generated during the CBE test. To investigate the wrinkling behaviour of the specimens, in addition to the front camera, the back of the test specimen was filmed by a smartphone camera at an oblique angle (about 20–30° from vertical). This oblique viewing angle was necessary to capture the three-dimensional nature of wrinkles, as wrinkles involve out-of-plane buckling that cannot be adequately observed from a perpendicular view. Most importantly, to obtain an accurate wrinkle onset angle, both front and back videos were aligned with the start time (time-synchronised).

An advantage of the CBE test is that bonding aluminium sheets to the lateral C Regions (see Fig. 6) enables the maintenance of an initial tow-stitch angle close to 90°, which represents the theoretical ideal for fabric shear testing. In contrast, the pre-shear angles of the UBE specimens prepared in this investigation varied from 1° to 4° due to the tension in the stitches. The CBE test's ability to maintain the initial tow-stitch angle at the theoretical optimum of 90˚ is a significant improvement (i.e., elimination of pre-shear [31]), providing more accurate and theoretically consistent results compared to the UBE tests, where pre-shear is unavoidable. However, unlike the UBE test, the CBE test does impose in-plane bending of the tows. Figure 6b highlights the in-plane bending areas in the CBE specimen (in the red and blue boxes). The CBE test also shows the formation of wrinkles, which are absent in the UBE test. The average wrinkle onset angle is 24.6˚±2.5˚. The wrinkles initiate at the B1 region (see red circled area in Fig. 6c) and then move to the A region. It has been found previously that wrinkling can induce a substantial overestimation (up to 20%) of the measured shear angle in the UBE test when using manual image analysis to interpret the test results [31]. As a result, the reported wrinkle onset angles in the CBE test may be overestimated, particularly in regions where significant wrinkling distorts the planar assumptions underlying angle extraction. Future use of anti-wrinkle plates may help delay wrinkle formation and improve the reliability of kinematic measurements.

Parallelogram Shear-Stretch (PSS) test

A relatively simple variation to the CBE specimen can be used to explore a very different region of the (shear angle) – (tensile stretching) parameter space. This involves cutting another octagonal specimen, eliminating deformation in Region B1 in the CBE specimen (Fig. 6a) by bonding aluminium foil to these regions. This creates homogenous deformation across the specimen (see Fig. 7 referred to here as the PSS test). To induce well-defined kinematics, the lateral edges of the PSS specimen were clamped and fixed to linear bearings that allow travel only in the vertical direction (see Fig. 7b). The region of interest in the PSS specimen is initially rectangular, with the tows oriented at 45° to the applied force. During deformation, the original shape of Region A transforms into a parallelogram (see Fig. 7b). Note, the PSS test entirely avoids in-plane bending of tows.

Figure 7b shows the dimensional changes of the PSS specimen due to the deformation. The strong boundary conditions of this test allow the theoretical kinematics to be derived. The theoretical shear angle, θ_A, is determined by the difference between the initial tow-stitch angle, $(2\Phi_A = \pi/2)$, and tow-stitch angle at a given displacement, $(\Phi_A + \omega_A)$, as predicted by Eq. (6).

$$\theta_A = \frac{\pi}{2} - \left[\frac{\pi}{4} + atan\left(\frac{L_0}{L_0 + \sqrt{2}D_A}\right)\right] \tag{6}$$

where, L_0 and D_A are the initial length of Region A (see Fig. 7) and the displacement of the machine crosshead, respectively. The theoretical engineering strain in the stitch direction during the PSS test, α_A, is calculated as a function of the displacement, see Eq. (7), where, ω_A is the changing angle between the tow and stitch directions with increasing machine crosshead displacement.

$$\alpha_A = \left[\frac{1}{\sqrt{2}\cos\omega_A} + \frac{D_A}{L_0 cos\,\omega_A}\right] - 1 \text{ with } \omega_A = \left(\frac{\pi}{4} - \theta_A\right) \tag{7}$$

The experimental engineering strain in the stitch direction during the PSS test, β_A, is calculated using Eq. (8). L_1 is the stitch length measured using ImageJ [30] at a desired displacement. A subsequent comparison between Eqs. (7) and (8) reveal how closely the PSS specimen follows this ideal kinematic prediction (see *'Kinematics'* section).

$$\beta_A = \frac{L_1 - L_0}{L_0} \tag{8}$$

Simple Shear (SS) test

A simple shear test (referred to here as the SS test) that samples yet another region of the (shear angle) – (tensile stretching) parameter space was designed by increasing the initial angle between the stitch and axial displacement direction to 90˚ (see Fig. 8a). The specimen was laterally fixed to vertically orientated linear guide carriages and bolted into the clamps along

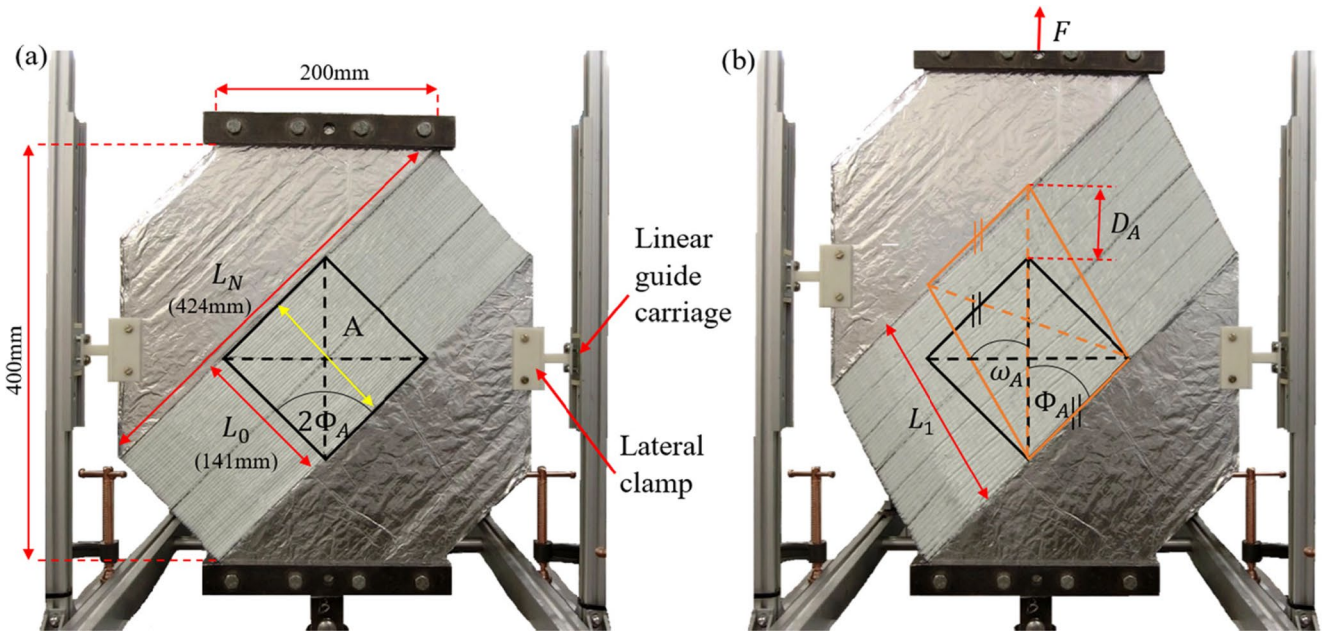

Fig. 7 PSS specimen with linear bearings (**a**) undeformed. The yellow arrow shows the initial direction of chain stitches (**b**), dimensional changes in the geometry during deformation (shape of Region A shifts from black square to orange parallelogram)

the upper right and lower left edges of the bonded regions (see Fig. 8). Again, the SS test avoids the in-plane bending of tows.

Figure 8b depicts the dimensional changes caused by deformation during the SS specimen. The theoretical shear angle, θ_s, of the SS test can be derived as a function of the machine displacement, D_B, and the initial specimen length, L_0', as shown in Eq. (9)

$$\theta_s = tan^{-1}\left(\frac{D_B}{L_0'}\right) \tag{9}$$

The theoretical engineering strain in the stitch direction during the SS test, α_s, is calculated as a function of the displacement, see Eq. (10).

$$\alpha_s = \frac{\left[\sqrt{(L_0')^2 + D_B^2}\right] - L_0'}{L_0'} \tag{10}$$

The experimental engineering strain in the stitch direction during the SS test, β_s, is calculated using Eq. (11) where, L_1' is the stitch length measured using ImageJ [30].

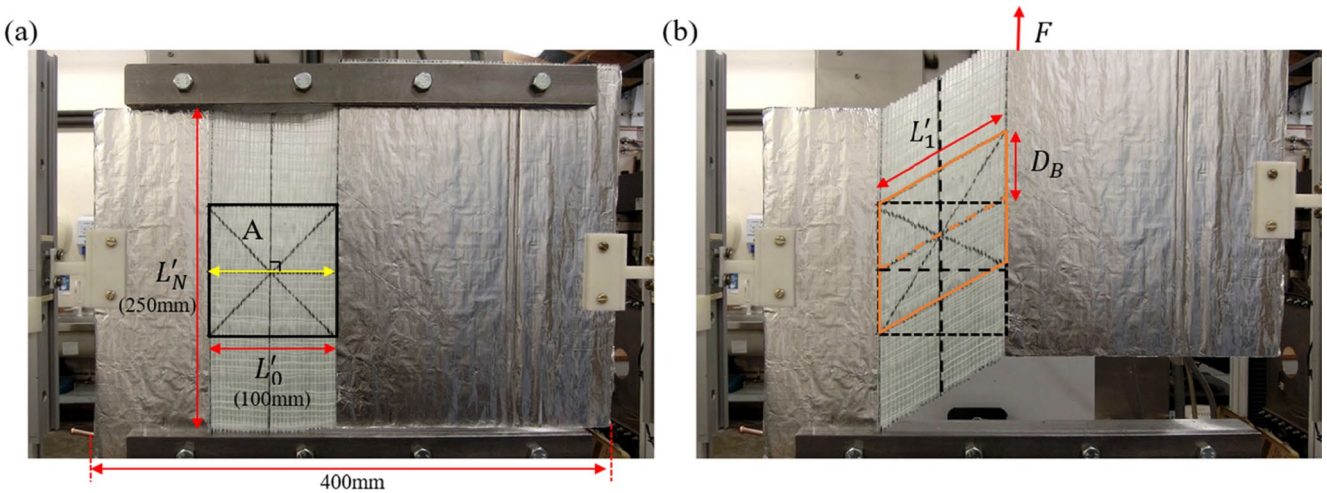

Fig. 8 Simple shear specimen with linear bearings (**a**) undeformed. The yellow arrow shows the initial direction of chain stitches (**b**) dimensional changes in the geometry during deformation. The shape of Region A shifts from a square (black) to a parallelogram (orange)

$$\beta_s = \frac{L_1' - L_0'}{L_0'} \tag{11}$$

As with the PSS test, a subsequent comparison between Eqs. (10) and (11) reveal how closely the experiments follow this ideal kinematic prediction (see *'Kinematics'* section).

Picture frame test with Pre-Stretching in stitch direction

The PF test, using pre-stretched pure-UDNCF specimens, also aims to provide insights into unexplored areas of the deformation space. The combined (i.e., low- and high-pressure boundary condition) G-clamp PF test method [15] was used to perform PF tests with pre-stretching along the stitch direction to a given percentage strain, before placing the specimen in the PF rig. Tests were performed with the intention of inducing three different stitch engineering strains: 5%, 10%, and 20%. First, a known length of pure-UDNCF was cut along the stitching direction. The fibre was then stretched by a certain percentage (e.g., a 30 cm length of stitches was carefully stretched along a straight line, perpendicular to the tow directions, until it reached 33 cm). Weights were placed around the extended fabric to maintain the stretch, and the outer lines of the specimen were marked with the specimen template. Figure 9a shows how the specimen returned to its original state after releasing the fabric's pre-stretch, compared to the template. Another template, with the dimensions of the PF specimen's central square region, was used to ensure the specimen was once again pre-stretched when clamped in the PF rig (see Fig. 9b). Note that, as with the unstretched PF test, pre-stretched PF test specimens also experience in-plane bending of the tows at the boundary, next to the rig clamps.

Results

Results from the various test methods are now discussed. First, the measured test kinematics are reported and compared against the theoretical kinematics (see the section *'Kinematics'*) before considering the measured forces. The latter are presented first in the section *'Force Measurements (2D Parameter Space)'* and next in the section *'Force Measurements (3D Parameter Space)'*. In the final part of the *'Results'* section, an attempt is made to interpret the force results and isolate the individual contributions to the total measured force from shear, stitch stretching and in-plane bending. Note that unintended pre-stretch in the stitch direction of the pure-UDNCF during handling affects the experimental results. The average number of tows in the tensile specimens was measured to be equal to the standard tow count of the fabric, i.e., 17 tows per 50 mm stitch length. In contrast, PSS and SS specimens showed approximately 8% and 6% pre-stretch, respectively. Furthermore, the PF specimens exhibited pre-stretch levels different from the initially intended values; specifically, the nominal pre-stretches of 0%, 5%, 10%, and 20% were measured as 1%, 12%, 15%, and 17%, respectively. Pre-stretch corrected test results are discussed in the following section (see [32] for details of the adjustment).

Kinematics

The kinematics from the various tests can be compared both with the corresponding theoretical predictions and with each other. Figure 10 shows that, as expected, both the measured shear angles in the UBE and CBE tests on pure-UDNCF are much lower than the theoretical prediction for ideal

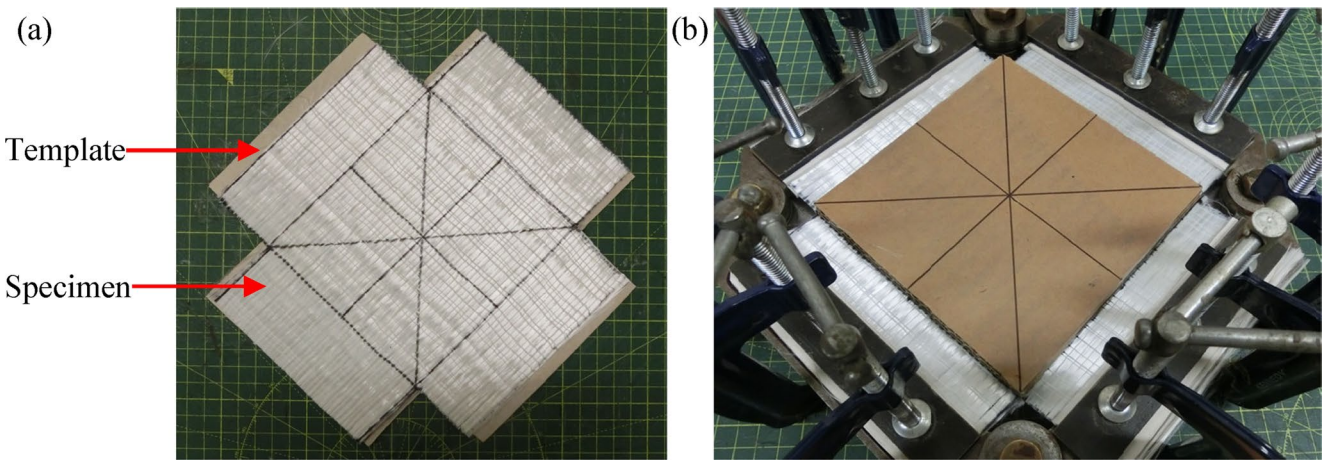

Fig. 9 (**a**) Comparison of dimensions of 10% pre-stretched PF specimen and the template (**b**) ensuring that the specimen is stretched precisely when mounting to the PF rig

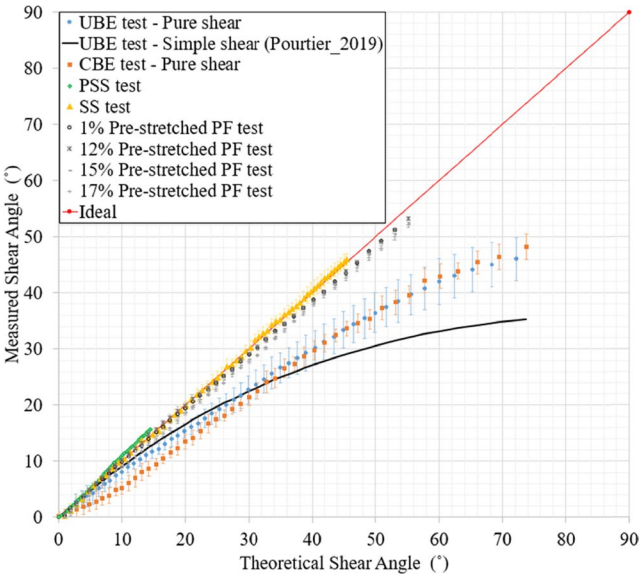

Fig. 10 Measured vs. theoretical shear angle average curves in A Region of each shear test. The error bars indicate +/- 1 standard deviation. The shear angle during simple shear (black line) has also been plotted versus the shear angle induced by pure shear using Eq. (5)

pin-jointed net (pure) shear kinematics [34]. The measured UBE shear angle lies closer to a simple shear prediction of Pourtier et al. [35] (see Eq. 5); the CBE shear angle is even lower, especially at low displacements.

Figure 11 shows the idealised deformation of a CBE test to explain the lower measured shear angle in the CBE test compared to the UBE test. Consideration of the possible kinematics accessible in the CBE test suggests that the imposed displacement can be accommodated by a combination of shear, stretching and in-plane bending. For a given

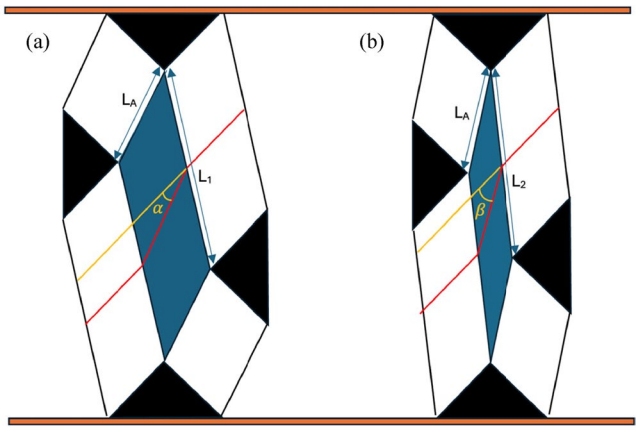

Fig. 11 Schematic of CBE test (**a**) with relatively low shear, low in-plane bending and high stitch stretch (**b**) with relatively high shear, high in-plane bending and low stitch stretch, both at the same axial displacement. The red line indicates the tow direction. L_1 and L_2 follow the stitch direction. The different deformations result in $L_1 > L_2$ and $\beta > \alpha$. The preferred deformation is determined through energy minimisation

displacement, the less the specimen shears, the more it needs to stretch in the stitch direction, and this also reduces the required amount of in-plane tow bending (see Fig. 11a). Clearly the minimum energy is a compromise between these three kinematics, though if the energy associated with in-plane bending is high, then scenario Fig. 11a is favoured over Fig. 11b. This potentially explains the low shear angle measured in the CBE test. Because the UBE specimen is much less constrained than the CBE specimen, it can shear more and stretch less without inducing in-plane bending. It does this by inducing relatively complex kinematics in the B regions, as shown in Figs. 5a&c, where the stitching fails to maintain fabric cohesion in Region B1, and Region B2 undergoes significant out-of-plane bending. In contrast, the kinematics in the B regions in the CBE test are more constrained, forcing the tows to bend in-plane, as shown in Fig. 6b.

Figure 12 shows a plot of the kinematics in each region of the CBE specimen. The shear angles in Regions B1 and B2 remain similar throughout the test and generally, are slightly greater than half the shear angle in Region A (see Fig. 12b). Both Region B2 and Region A undergo similar amounts of stretching in the stitch direction (see Fig. 12c). In contrast, the boundary conditions in Region B1 largely mitigate stitch strain, which remains close to zero throughout the test (see Fig. 12c). Therefore, while each of the three deformable regions within this specimen is subject to different combinations of shear and stretching along the stitch direction, the uniformity of the strain field in each region means analysis of the different contributions to the total measured force in this test may be feasible. Theoretical analysis, to determine the separate contributions of Regions A, B1 & B2 to the measured axial force, is challenging due to the complexity of the sample kinematics (much more than for biaxial fabrics, e.g [40])., however, the test will be useful for evaluating numerical predictions at a later stage, after an appropriate constitutive model is implemented in a FEA code. In the meantime, the CBE test provides a kinematically better-defined test when compared to the UBE test, for this type of fabric. The CBE test result also provides further evidence regarding the origins of the various contributions to the measured axial force (as discussed further in the *'Force Measurements'* section).

Turning to the SS and PSS tests, their measured average shear angle curves are also plotted in Fig. 13. Both results are seen to closely follow their theoretically predicted kinematics, determined using Eqs. (6) and (9). The SS test achieves higher shear angles ($\approx 45^\circ$) than the PSS test ($\approx 15^\circ$) before specimen failure. The theoretical and experimental tensile strains in the stitch direction for the PSS specimens were calculated using Eqs. (7) and (8), and for the SS specimens using Eqs. (10) and (11). As shown in Fig. 13a, values

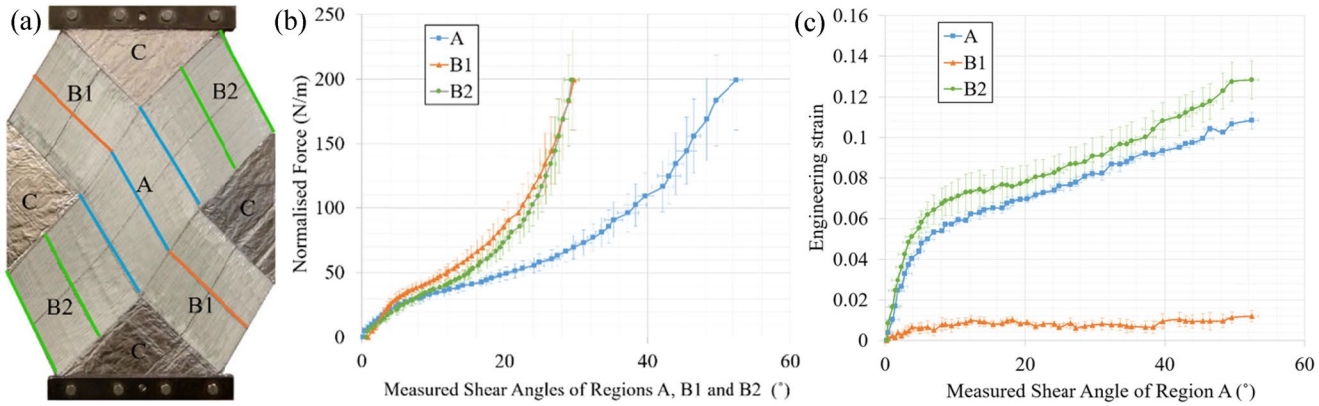

Fig. 12 (**a**) Deformed CBE specimen, the coloured lines indicate the stretching measurements from each Region (blue, orange, and green lines for the A, B1, and B2 Regions, respectively) (**b**) normalised axial force vs. measured shear angle of Region A, B1 and B2 (**c**) engineering strain vs. measured shear angle of Region A

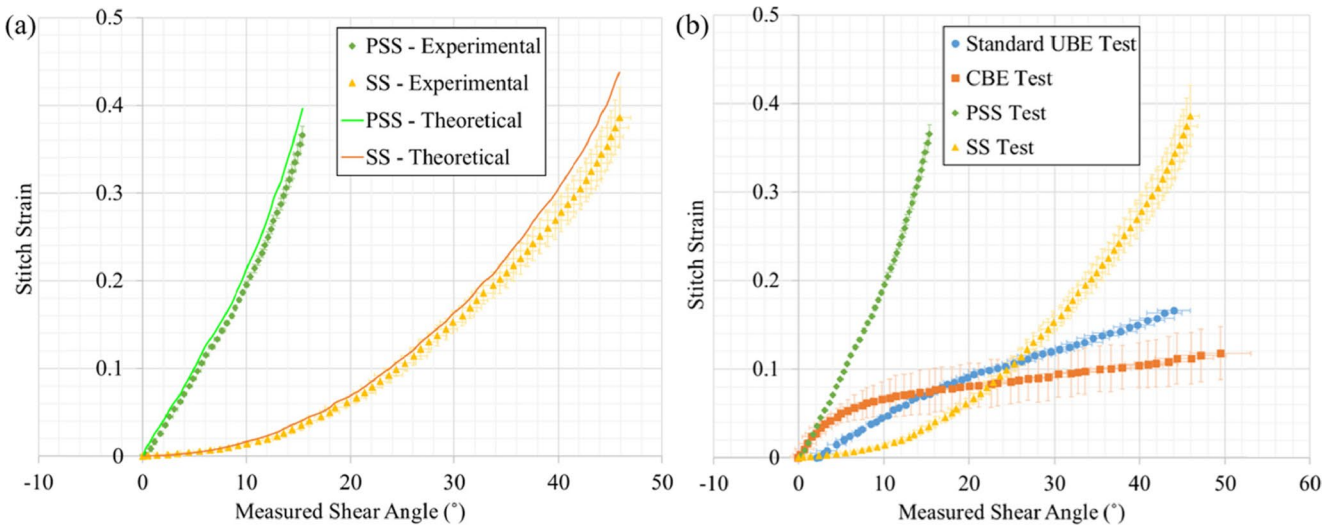

Fig. 13 (**a**) Comparison of the average theoretical and experimental stitch strains in Region A of the PSS & SS specimens (**b**) experimental stitch strain in Region A vs. measured shear angle curves in different tests. The error bars indicate +/−1 standard deviation of four specimens

obtained from theoretical equations match closely with the measured strain in the stitch direction, demonstrating that the fabric kinematics of the PSS and SS tests are well-defined. Figure 13b shows the experimental stitch strain in Region A vs. the measured shear angle curves in different shear tests. The PSS test shows much greater stretch in the stitch direction across all shear angles than the UBE and CBE tests, while in the SS test, the stretch in the stitch direction exceeds that occurring in the UBE and CBE tests only after around 25° of shear.

Considering the PF test specimens, the shear angle kinematics of all these tests, with both pre-stretched (i.e., 12%, 15%, and 17%) and unstretched (~1% pre-stretched) specimens, are seen to lie close to the ideal pure shear prediction in Fig. 10. This pure shear kinematic means that the stretch in the stitch direction remains constant with shear angle and is determined by the pre-stretching levels imposed at the start of each test. Given the stitch strain versus shear angle data shown in Fig. 13b (and also given the strain in the pre-stretched PF tests), it is possible to estimate the engineering strain acting perpendicular to the tows during the PF, UBE and CBE tests, using Eq. (12). This strain is referred to here as the in-plane transverse tow strain, ϵ_{trans}.

$$\epsilon_{trans} = (\beta + 1)\cos\theta - 1 \tag{12}$$

where β is the engineering strain in the stitch direction and θ is the shear angle in the specimen. Figure 14 shows that the unstretched PF test induces an increasingly compressive (negative) in-plane transverse tow strain, right from the start of the test, as the shear angle increases. In contrast, specimens in the PF tests with pre-stretch of the stitching, the CBE test, and the UBE test all initially undergo a positive tensile in-plane transverse tow strain. This strain only

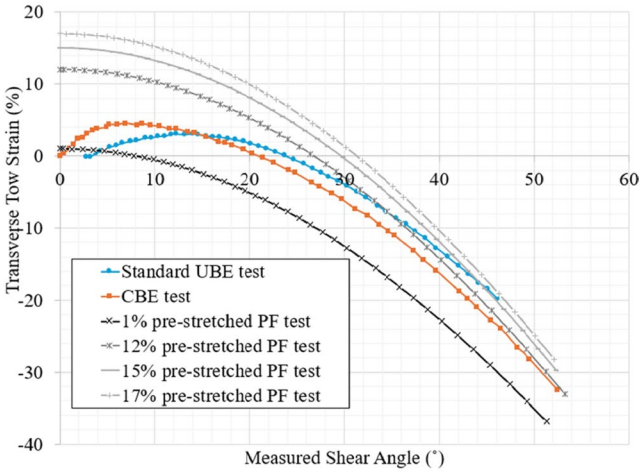

Fig. 14 Transverse tow strain in the UBE, CBE and PF specimens versus measured shear angle

becomes compressive in these tests, after around 20° to 30° of shear (see Fig. 14). This behaviour is useful in understanding the contributions to the measured axial force from the various deformation kinematics acting in the different tests.

Before presenting the normalised axial forces measured in each of these tests, it is useful to summarise the deformation kinematics that could potentially contribute to the measured force in each test at low shear angles (see Table 1).

- The tensile test produces only one contribution: tensile stretching of the stitch (see Fig. 2),
- The UBE test produces just two contributions at low shear angles: shear and stretching of the stitch (see Fig. 5c). Compressive transverse tow strain only begins at higher shear angles (see Fig. 14).
- The PF test (unstretched) creates three contributions: shear, in-plane bending (see Fig. 5d&e) and a gradually increasing compressive transverse tow strain with increasing shear angle (see Fig. 14).
- The CBE test is similar to the UBE test, but this time produces three contributions: shear, stretching of the stitches and in-plane bending (see Fig. 6b). Compressive transverse tow strain only occurs at shear angles greater than ~20°, see Fig. 14.
- The PSS and SS tests both include just two contributions: shear and stretching of the stitch. There is no contribution from in-plane bending of the tows because they remain perfectly straight during the tests (see Figs. 7 and 8). Compressive transverse tow strain is also absent throughout these tests.
- The PF test (with pre-stretch) creates just two contributions at low shear angles: shear and in-plane bending. The pre-stretching of the specimens ensures that compressive transverse tow strain only occurs at higher shear angles.

Force measurements (2D parameter Space)

Figure 15 ignores the strain in the stitch direction and therefore only provides a partial view of the overall behaviour. Nevertheless, it is included as it does allow a direct comparison of the normalised axial force versus shear angle for each of the tests. For the UBE (see Fig. 5a) and CBE (see Fig. 6) tests, the axial force was normalised by dividing the length of Region A of each specimen, whereas for the PSS and SS tests, the axial force was divided by the effective length of the specimen in the tow direction, i.e. L_N (see Fig. 7a) and L'_N (see Fig. 8a), respectively (though discussion of the SS and PSS test results is deferred to the next section). For the PF tests, the axial force was divided by the side length of the PF rig.

Despite work to mitigate the adverse influence of the strong boundary conditions of the PF test due to misalignment errors [15] and also due to friction in the PF rig [32], the normalised force measured in the standard UBE test was consistently and reliably measured to be much lower than that measured in the PF test (see Fig. 15a). The friction-modified PF test result is higher by a factor of 5 at 5˚, 2 at 10˚ and 1.5 at 30˚. This difference is significant and not usually observed when characterising the forming behaviour of biaxial woven fabrics or biaxial NCFs. Several explanations can be proposed to explain this difference:

1. Meso-scale slip mechanisms acting between the tows and the stitching, possibly operate in the UBE test but not in the PF test,

Table 1 Kinematics potentially contributing to the measured axial force in each test

Test	Tensile stretching of the stitches	Shear	In-plane bending	Compressive transverse tow strain at less than 25°
Tensile	✓	-	-	-
UBE	✓	✓	-	-
PF (unstretched)		✓	✓	✓
CBE	✓	✓	✓	-
PSS	✓	✓	-	-
SS	✓	✓	-	-
Pre-Stretched PF	-	✓	✓	-

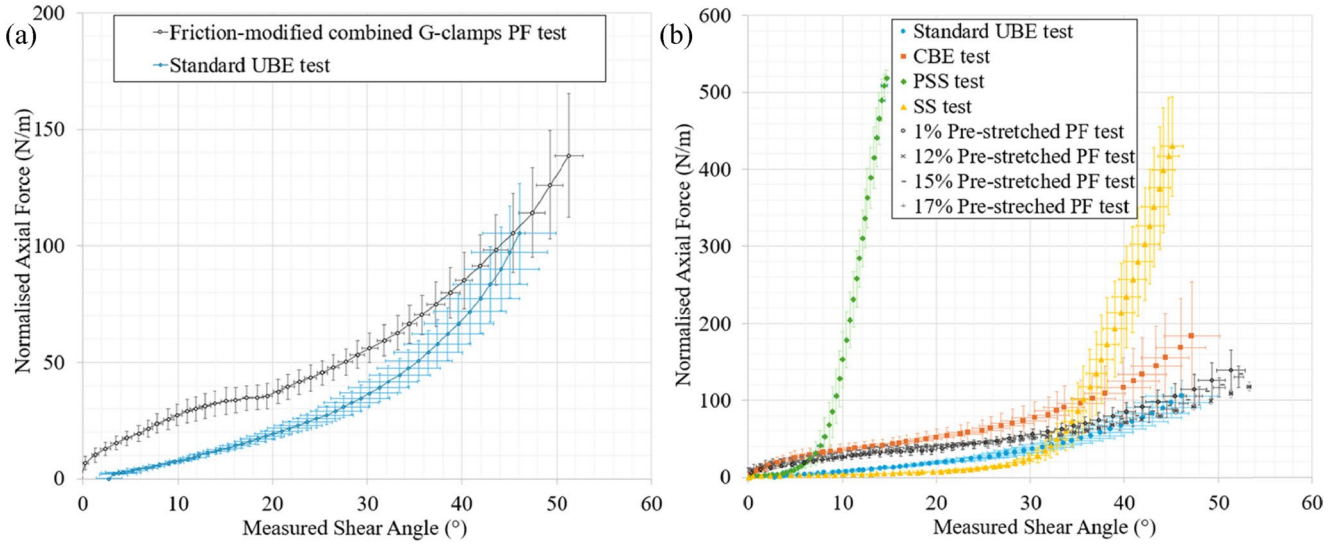

Fig. 15 (**a**) Comparison of normalised axial force vs. measured shear angle curves of the standard UBE test and friction-modified combined G-clamps PF test curves (**b**) Normalised axial force vs. measured shear angle of the different shear tests. The error bars indicate +/- 1 standard deviation of four specimens

2. The gradually increasing in-plane transverse compression of the tows in the PF test (see Fig. 14), leads to significant compressive stresses in the fabric; these are absent in the UBE test,
3. Extension in the stitch direction reduces the shear resistance of the fabric in the UBE tests,
4. In-plane bending contributes very little to the measured force in the UBE test (see Fig. 4c) but does make a significant contribution to the force measured in the PF test (see Fig. 4d&e).

Some of these explanations can be quickly discounted. Regarding (I), close inspection of the fabric during testing showed no evidence of slip between the tows and stitching, with the highly extensible stitching moving with the tows, stretching rather than slipping (see Video 1). Regarding (II), it is clear from Figs. 10 and 13b that the UBE specimen undergoes considerable positive stitch strain, while the PF specimens undergo pure shear (no stretching of the stitches) and consequently experience an increasingly compressive (negative) transverse strain across the tows, see Fig. 14. This compressive transverse tow strain could potentially account for the higher axial force measured in the PF test. However, on close inspection, it is seen that the CBE, and the pre-stretched PF tests also show much higher forces than the UBE test at low shear angles, despite being free from compressive transverse strains until at least 25° of shear (see Fig. 14), suggesting that compressive transverse tow strain is not the reason for the higher axials force measured in the PF test.

This leaves explanations (III) and (IV). In Kahavita et al. [15], explanation (III) was assumed to be a likely reason for the relatively low normalised axial force measured in the UBE test; however, explanation (IV), a significant energy contribution from in-plane bending in the PF test, was not considered. As mentioned, Fig. 15b shows that the CBE test produces significantly higher normalised axial forces than UBE specimens. While this can be partly attributed to greater contribution from Regions B1 & B2 (see Fig. 6) in the CBE test, compared to the UBE test (see Fig. 5a), the much higher in-plane bending induced in the CBE test (see Fig. 6b) is thought to play a role. Furthermore, at low shear angles, all the pre-stretched PF specimens show higher forces than the UBE curve, despite the lack of compressive transverse strains (see Fig. 14), this is again presumably due to the contribution from in-plane bending of tows.

Force measurements (3D parameter Space)

The normalised force results are better understood when presented in a 3D plot within the (shear angle) – (tensile stretching) parameter space (see Fig. 16) and provide further evidence for the in-plane bending contribution to the measured force in certain tests. Only tests with homogenous kinematics throughout the test sample are plotted in this figure to make subsequent analysis of the results in the next section possible. The normalised tensile test force results lie at one extreme of the graph, as there is no shearing during the test, whereas all the other test results are spread throughout the 3D parameter space. When viewed in this 3D format, the reason for the sudden increase in the measured axial force in the SS and PSS tests is clear, both induce significant stretching of the stitching, the PSS at relatively low shear angles and the SS test at higher shear angles. Figure 16 shows that pre-stretching of the fabric has little effect on the measured force in the PF (pre-stretched) tests. This supports the conclusion that transverse compression of

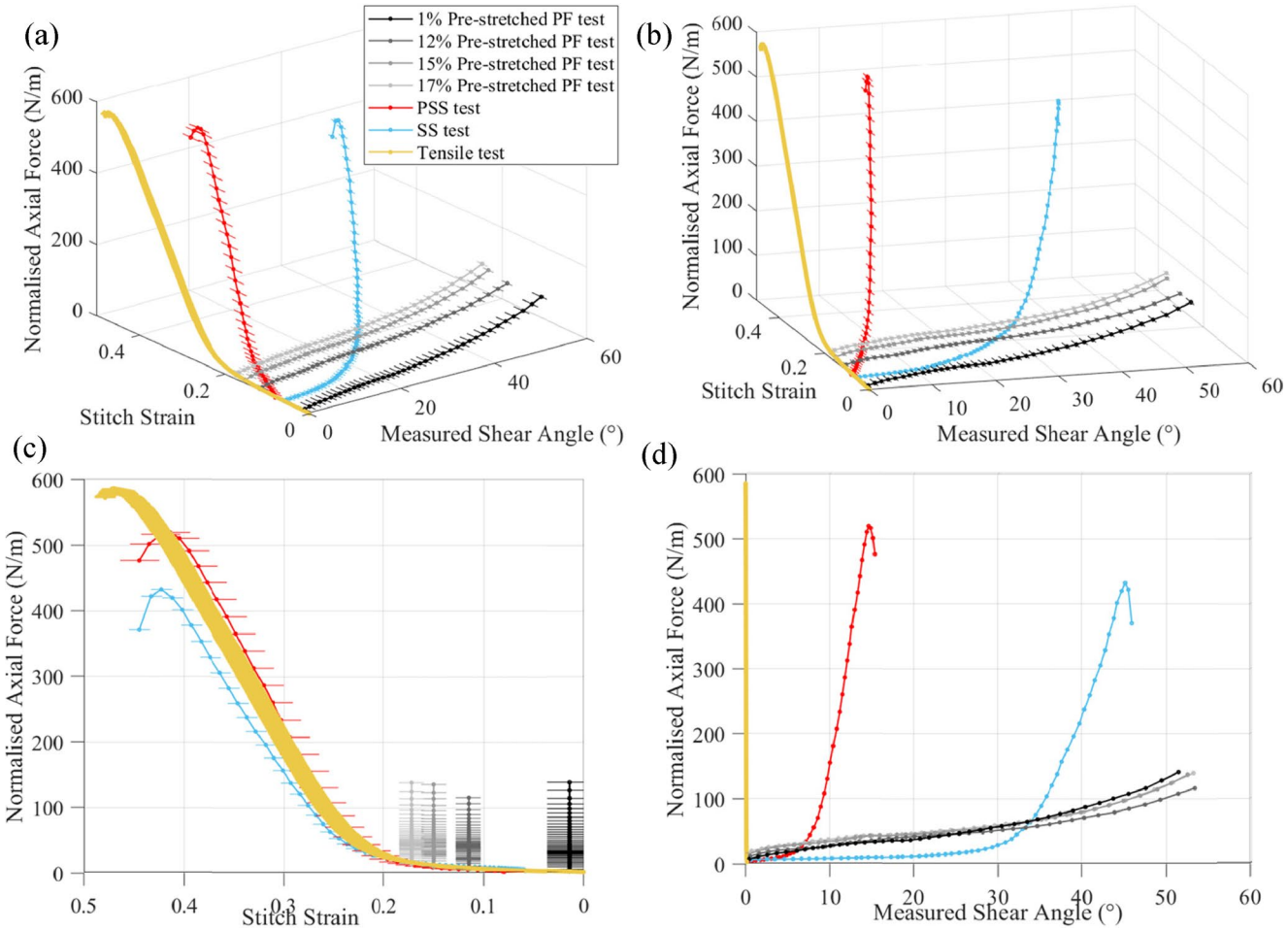

Fig. 16 (**a**)-(**d**) Normalised axial force vs. measured shear angle and stitch strain from various shear and tensile testing data. The same 3D graph is shown from different angles

the tows is not the reason for the relatively high axial force measured in PF tests. Also, for a given shear angle, the measured force decreases slightly with increasing pre-stretch; this is expected if the majority of the force is generated by in-plane bending, as the pre-stretched specimens contain fewer tows per unit length. The fact that the SS curve travels far below all the pre-stretched PF test results (i.e. the same macro-strain state in terms of shear angle and stitch stretch generates much less force) is important and suggests that something other than stitch strain or fabric shear creates the higher forces in the PF tests. This extra contribution is again thought to come from in-plane bending, which is absent from the SS test but present in the PF (pre-stretched) tests.

Isolating the Tensile, shear and In-Plane bending contributions

The presented evidence strongly suggests that tensile stretching, shear, and in-plane bending all contribute to the total measured axial force to different degrees in these tests. The challenge is to isolate the separate contributions and estimate the behaviour of each of the various stiffnesses as a function of both shear angle and tensile stretching in the stitch direction. Due to the sparsity of the data, various assumptions are used to isolate the three force contributions, making reasonable intuitive estimates of the likely behaviour of the shear, stitch tensile and in-plane bending contributions to the axial force measured in the experiments. The stitch tensile component is estimated directly from independent tensile tests on specimens aligned with the stitch direction, the shear component is inferred from shear-dominated tests (PSS and SS), and the in-plane bending component is estimated from the PF test. These estimates are then evaluated based on: (i) expected behaviour and (ii) their predictive capacity. Note that this is not a fitting process; rather, the behaviour is postulated and compared against the sparse dataset measured by the various tests. The approach of estimating the material behaviour requires anticipating how each contribution (shear & tensile load in the stitch direction, and in-plane bending) acts along the axial direction.

In the following discussion, the term 'material system' refers to the material's local non-orthogonal reference frame, with one basis pointed along the tow direction and the other along the stitch direction. The 'machine system' refers to the machine's (orthogonal) reference frame with one basis directed along the axial travel direction. The first step of the approximation process involves generating a 3D polynomial surface for the 2D tensile experimental data, i.e., predicting how the tensile data varies with increasing shear angle. To achieve this, a polynomial surface is created using three estimates. The first assumes no coupling between tensile and shear stiffness, resulting in a constant surface extending along the measured shear angle direction. Alternatively, either a linearly increasing or decreasing coupling between tensile stiffness and shear can be assumed, yielding surfaces that either decrease or increase with the shear angle. Selecting the most accurate tensile surface is a critical step in this approximation process since all the results, including the inherent shear surface, follow from the initial guess of the tensile surface. These different attempts are discussed in detail in [32]. The following presents a summary of the most successful approach (arrived at after several iterations), namely, a small linear increase in tensile force as shear angle increases (see Fig. 17), (here, orange dots show the measured tensile test data). Note the use of the term 'inherent' in the graph. This is meant to infer that the contribution of an isolated deformation mode, in this case, tensile stretching in the stitch direction, is estimated in the non-orthogonal 'material' system. This can then be normalised and expressed in the axial direction to determine the 'inherent normalised axial force'.

Using this estimate of the inherent tensile data, $F_{t\theta}$, the component of the stitch tensile force acting along the machine axial loading direction for the two tests: (i) SS (Eq. 17, see Appendix A), and (ii) PSS (Eq. 22, see Appendix A) was calculated and then subtracted from the measured (normalised) axial force data for the two tests, to obtain the shear contribution to the measured axial force (Eq. 19 for the SS test and Eq. 24 for the PSS test). The normalised axial force due to shear was then transformed back to the material system (Eq. 20 for the SS test and Eq. 26 for the PSS test), and these are plotted in Fig. 18 (see Appendix A for derivations of these equations). In the tensile test, the shear force is zero and can be plotted along the stitch strain direction (red dots shown in Fig. 18). A simple polynomial surface is then created to approximate the inherent shear data from all three tests (see Fig. 18b). The simple polynomial surface representing the inherent shear force is a reasonable fit to the SS data but a poor fit to the PSS measured data, suggesting that the PSS data likely involved nonlinearities or interactions between tensile and shear behaviours that are not well-represented by this simple approximation.

Despite this poor fit with the PSS data, the approximation process is continued. Figure 19 compares the postulated inherent shear surface (Fig. 19b) with the experimental data from the PF test. Due to the force contribution expected from in-plane bending, the PF tests produce larger forces than the inherent shear surface. The inherent shear surface is considered an uncertain but reasonable representation at this stage and suggests that in-plane bending creates a considerable contribution to the normalised axial force of the PF test.

Returning to the approximation process, the polynomial equation of the shear surface plotted in Fig. 19 is used to estimate the normalised shear force in the machine system of each PF test (F_{MS}, pink dots shown in Fig. 20a), for the four pre-stretching levels of 1%, 12%, 15% and 17% using Eq. 13 (similar to Eq. 3 in [15]).

$$F_{MS} = \frac{F_{IS}}{2\cos\left(\frac{\varnothing}{2}\right)} \tag{13}$$

where F_{IS} and $\varnothing$ represent the normalised material shear force in the tow direction (from the polynomial equation of the shear surface plotted in Fig. 18b), and the frame angle, respectively. The surface polynomial fitted to the shear data in the PF test and transformed to the axial loading direction is shown by the gold colour in Fig. 20a. The green surface in Fig. 20a represents the polynomial surface created from the PF test experimental data. The in-plane bending surface of the PF test machine system (Fig. 20, blue) was obtained by subtracting the shear surface (Fig. 20a, gold) from the PF test experimental surface (Fig. 20a, green). Figure 20a suggests the shear contribution to the machine axial load is significantly lower than the in-plane bending contribution of the 1% pre-stretched PF test. In this scenario, a majority of the axial force measured in the PF test on this pure-UDNCF

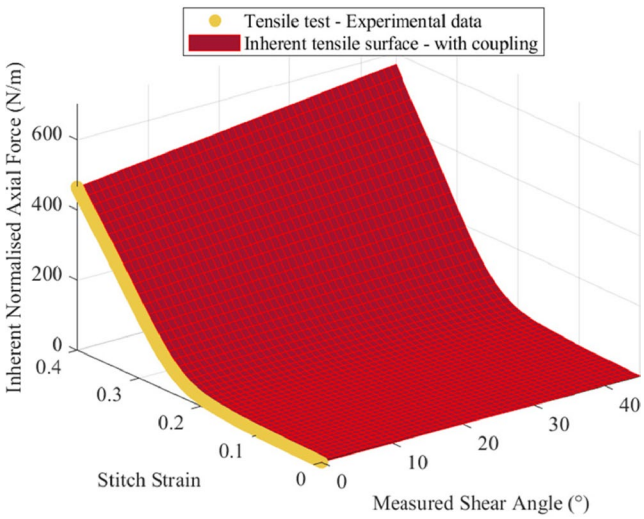

Fig. 17 Proposed inherent tensile surface with a linear coupling

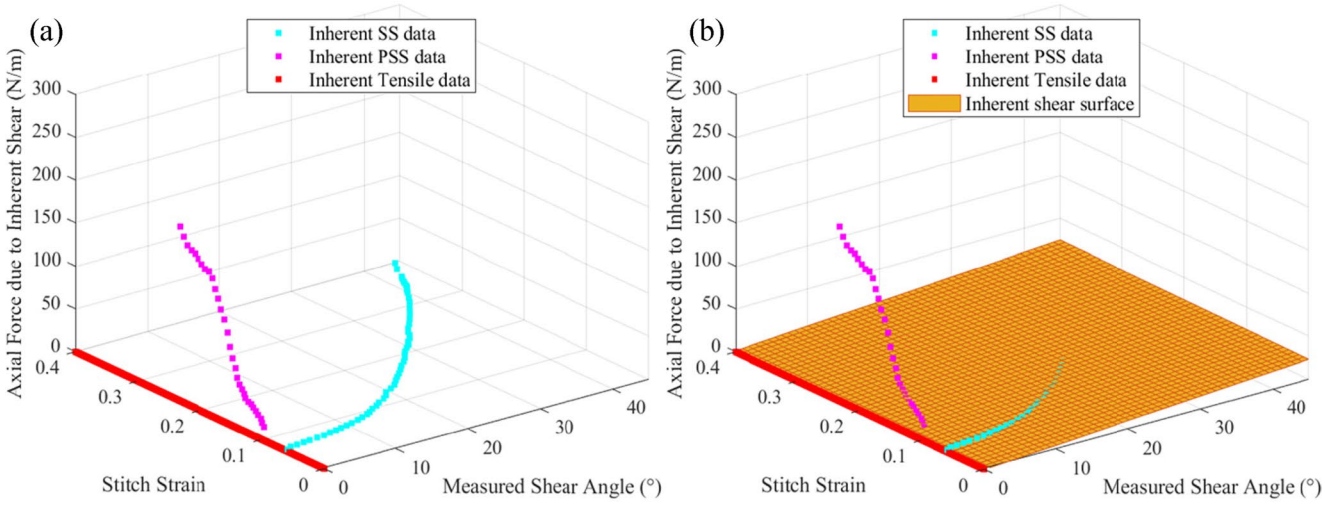

Fig. 18 The normalised axial force due to the inherent shear behaviour of the fabric as a function of shear angle and stitch strain (**a**) inherent shear data (**b**) inherent shear data with a fitted shear surface

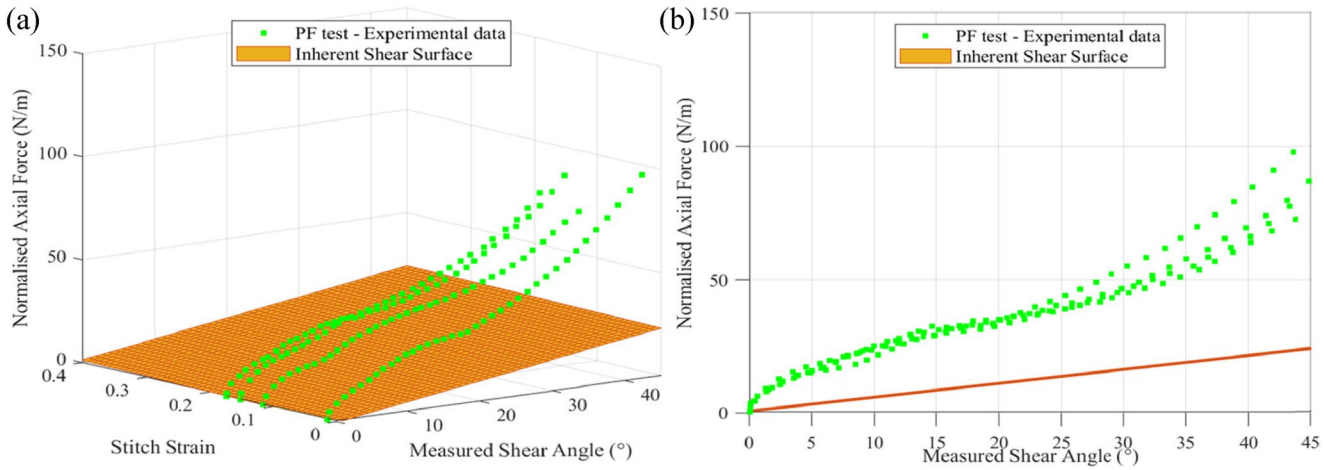

Fig. 19 A Comparison of inherent shear surface and PF test experimental data, (**a**) and (**b**) the same graph is shown from different perspectives

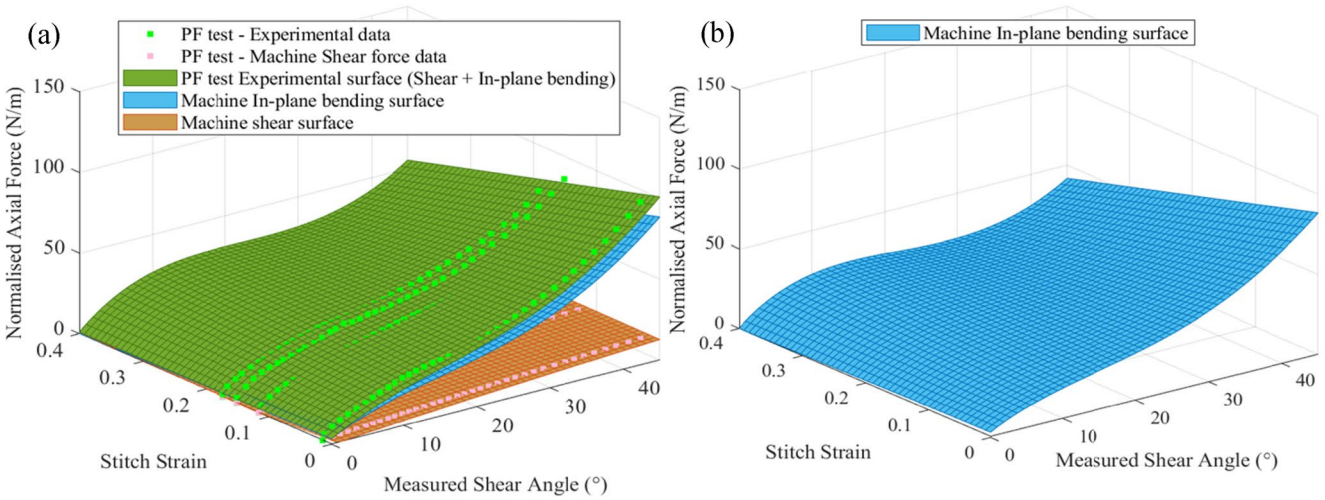

Fig. 20 (**a**) Comparison of three surfaces of the PF test machine system (**b**) machine In-plane bending surface

is contributed by the in-plane bending stiffness rather than due to the fabric's shear stiffness.

The next step is to convert the in-plane bending surface in the machine system (F_I) into the material system (i.e., acting along the tow direction). This can be achieved by applying Eq. 15 and assuming that in the PF test, the in-plane bending contribution to the measured axial force varies with the shear angle in the same way as the shear contribution does.

$$F_I = \frac{F_{II}}{2\cos\left(\frac{\varnothing}{2}\right)} \tag{14}$$

$$F_{II} = F_I * 2\cos\left(\frac{\varnothing}{2}\right) \tag{15}$$

where, F_{II} and $\varnothing$ represent the normalised inherent in-plane bending force and the frame angle at a given displacement, respectively. Figure 21 shows the resultant in-plane bending surface in the inherent system. Table 2 in Appendix B shows the polynomial coefficients of each surface created using this approximation process.

Using these various approximations, a comparison of the measured machine data and the prediction of the combined contributions, when converted from the material system to the machine system, can be made. i.e., using the three proposed surfaces (Figs. 17, 18b and 21). Strong agreement found in making this comparison (Figs. 22, 23, 24 and 25) suggests that the assumption that most of the force in the PF test is due to in-plane bending is reasonable for this particular fabric.

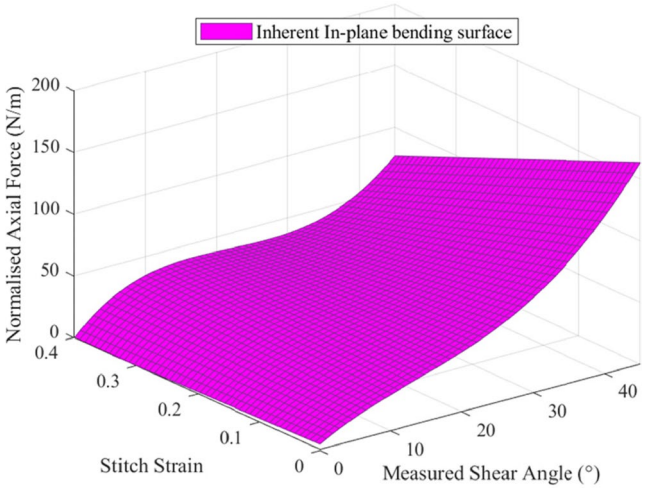

Fig. 21 In-plane bending surface in the inherent system

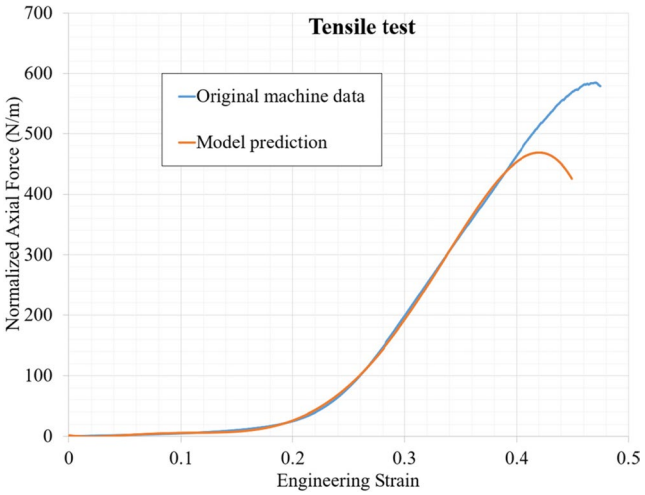

Fig. 22 Comparison of original machine data and model prediction of the tensile test

Conclusions

Characterisation tests have been designed to generate well-defined kinematics with different combinations of shear, stitch tensile strain and in-plane bending modes for pure-unidirectional non-crimp fabric (pure-UDNCF). Evidence from these tests, including: (i) the relatively low shear angle measured in the CBE test compared to the UBE test, (ii) the relatively low axial force measured in the UBE test compared to the PF tests [15], and (iii) the relatively low axial force measured in the SS test compared to the PF tests, all point towards a significant contribution from in-plane bending kinematics to the measured axial force in certain tests, namely the PF and CBE tests. Based on this conclusion, an attempt to isolate the size of the shear, stitch stretch, and in-plane bending contributions of the pure-UDNCF has been made. Despite the sparsity of data and the use of several intuitive assumptions, when fed back into the relevant equations, the approximated behaviours, represented by simple polynomial surface functions, provide good comparisons with experimental results (see Figs. 22, 23, 24 and 25). The findings suggest that for this fabric, the contribution of in-plane bending is significantly higher than that of shear in the PF test. While the CBE test is not directly used to identify the different force contributions from shear, stretching and in-plane bending, its well-defined kinematics make it a suitable test for evaluation of constitutive models that include these three distinct stiffnesses (prior to using such models in complex forming simulations). To the author's knowledge, this is the first time the contribution to the measured force from in-plane bending has been computed.

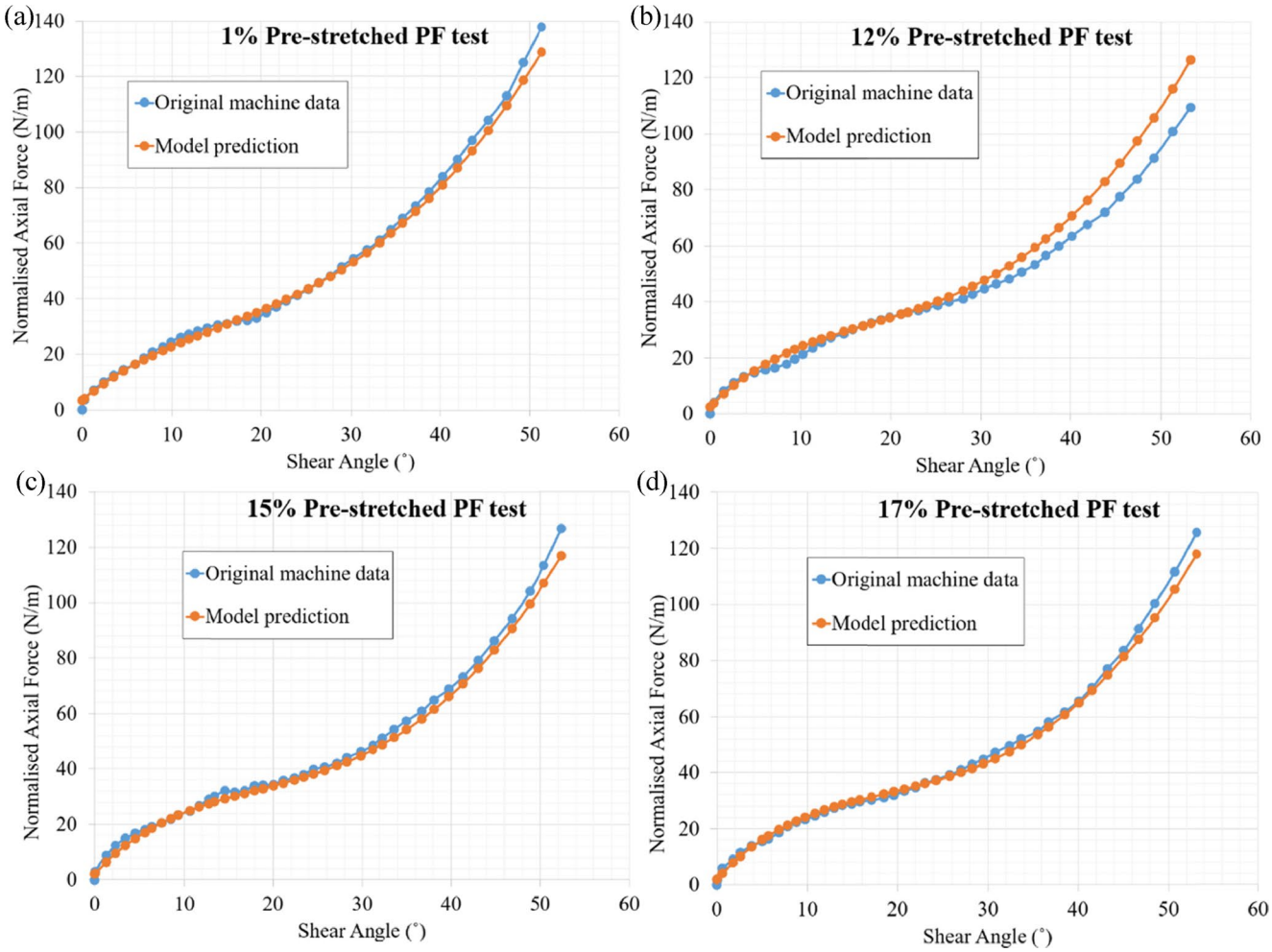

Fig. 23 Comparison of original machine data and model prediction of the picture frame test with different stretching percentages (**a**) 1% (**b**) 12% (**c**) 15% (**d**) 17%

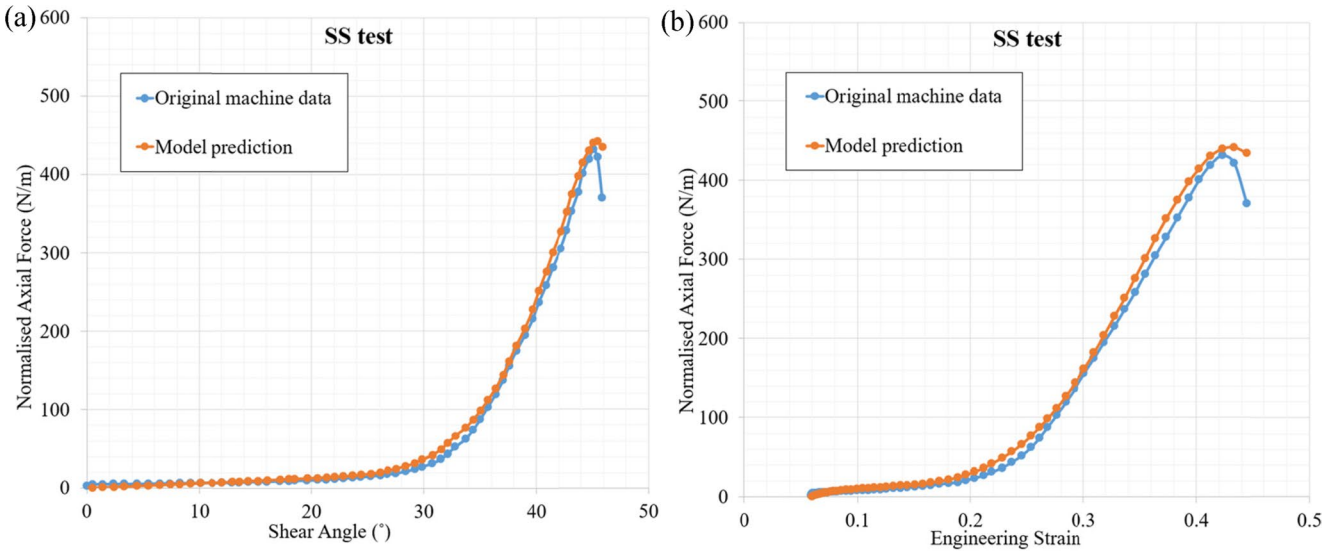

Fig. 24 Comparison of original machine data and model prediction of SS test (**a**) normalised axial force vs. measured shear angle (**b**) normalised axial force vs. engineering strain

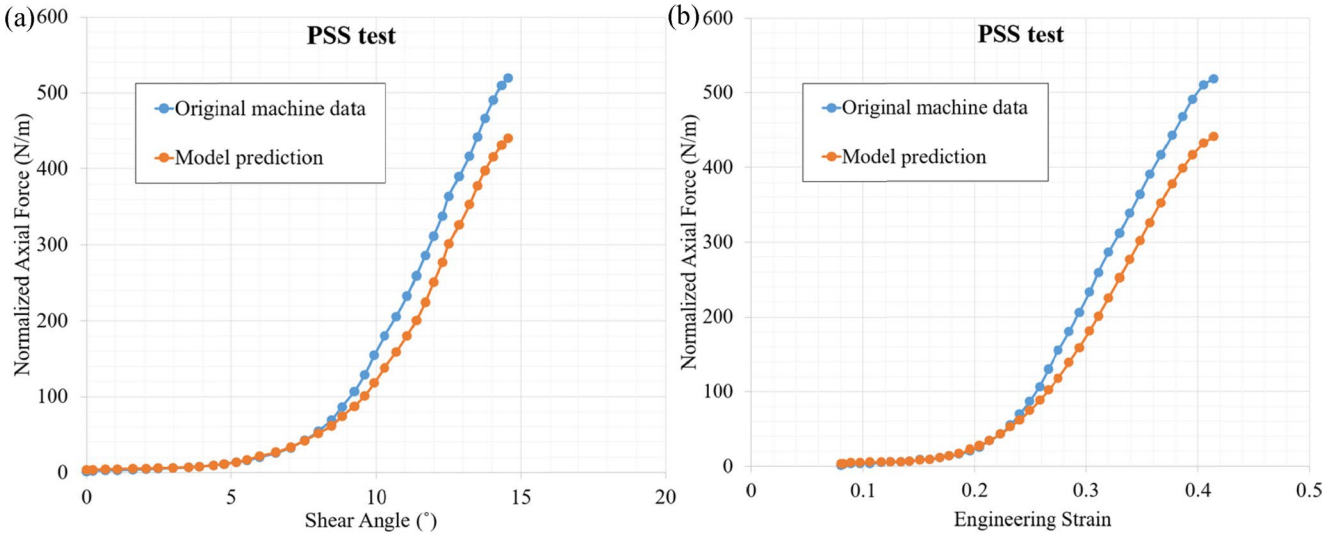

Fig. 25 Comparison of original machine data and machine prediction of PSS test (**a**) normalised axial force vs. measured shear angle (**b**) normalised axial force vs. engineering strain

Appendix A

Determining the stitch tensile force acting along the machine axial loading direction for the SS and PSS tests.

In the SS test, the material shear direction acts co-linearly with the machine's axial loading direction throughout the test, while the stitch tensile load direction acts at a changing angle, ω_A, to the machine's axial loading direction (see Fig. 26 a). In the PSS test, neither the material shear direction along the tows nor the tensile stretching along the stitch direction are orientated co-linear with the machine's axial loading direction (see Fig. 26 b), and so both the relevant force components acting in the machine's axial loading direction must be determined.

According to Fig. 26 a

$$\omega_A = \frac{\pi}{2} - \theta_A \tag{A1}$$

$$F_{at\theta} = F_{t\theta} \cos\left(\frac{\pi}{2} - \theta_A\right) \tag{A2}$$

where, $F_{at\theta}$ is the axial force due to tension along the stitch direction, at a given shear angle θ_A measured in the machine's axial loading direction and $F_{t\theta}$ is the tensile force per unit length measured in the stitch direction and is given by the polynomial shown in Fig. 17. The total axial machine force per unit length measured in the SS test is,

$$\underbrace{F_{at\theta} + F_{as\theta}}_{\text{Measured data (normalised axial force of SS test)}} = F_{t\theta} \cos\left(\frac{\pi}{2} - \theta_A\right) + F_s \tag{A3}$$

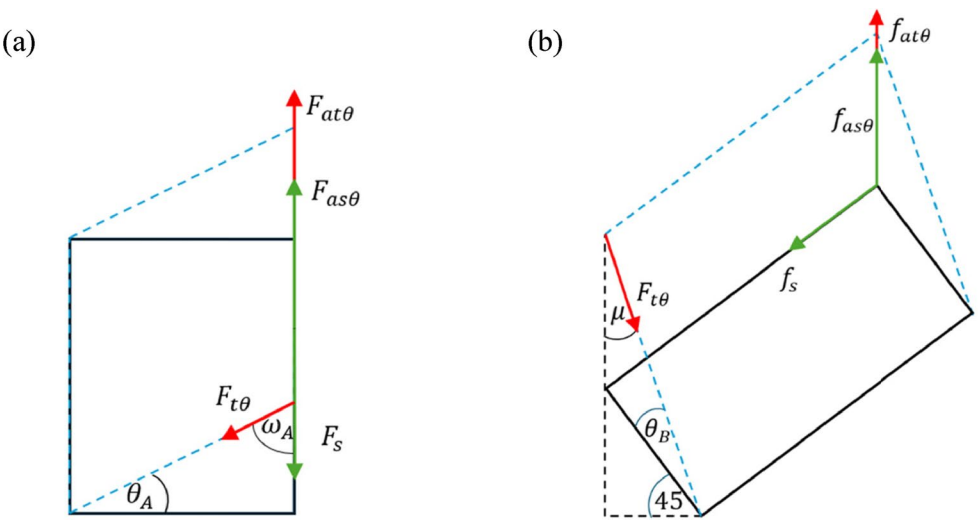

Fig. 26 The forces acting on the specimen during deformation (**a**) SS (**b**) PSS

where for the SS test,

$$F_s = F_{as\theta} \tag{A4}$$

Here, $F_{as\theta}$ is the axial machine force attributable to fabric shear and F_s is the material shear force per unit length acting along the tow direction. Thus,

$$F_s = F_{at\theta} + F_{as\theta} - F_{t\theta}\cos\left(\frac{\pi}{2} - \theta_A\right) \tag{A5}$$

According to Fig. 26 b,

$$\mu = \frac{\pi}{4} - \theta_B \tag{A6}$$

$$f_{at\theta} = F_{t\theta}\cos\left(\frac{\pi}{4} - \theta_B\right) \tag{A7}$$

Here μ is the angle between the machine's axial loading direction and the stitch direction, $f_{at\theta}$ is the force due to tension in the stitch direction, acting along the machine's axial loading direction at a given shear angle θ_B, and $F_{t\theta}$ is the tensile force per unit length acting along the stitch direction and is given by the polynomial shown in Fig. 17.

The direction of the shear force due to fabric shear doesn't change during the test. For the PSS test,

$$f_{as\theta} = f_s\cos\left(\frac{\pi}{4}\right) \tag{A8}$$

Therefore,

$$f_s = \sqrt{2}f_{as\theta} \tag{A9}$$

The total axial machine force per unit length measured in the PSS test is,

$$\underbrace{f_{at\theta} + f_{as\theta}}_{\text{Measured data (normalised axial force of PSS test)}} = F_{t\theta}\cos\left(\frac{\pi}{4} - \theta_B\right) + \frac{f_s}{\sqrt{2}} \tag{A10}$$

where, $f_{as\theta}$ is the force acting along the machine's axial loading direction due to fabric shear and f_s is the shear force per unit length acting along the tow direction. Thus,

$$f_s = \sqrt{2}\left(f_{at\theta} + f_{as\theta} - F_{t\theta}\cos\left[\frac{\pi}{4} - \theta_B\right]\right) \tag{A11}$$

Appendix B

Fitted polynomial surface coefficients.

Table 2 Polynomial coefficients of each surface created. Note that in these equations, x and y represent the measured shear angle and stitch strain, respectively

Surface	Coefficients
Inherent tensile surface with coupling (Fig. 17) $F(x,y) =$	2.21217227554466–0.0623886735663608 x −238.075195972052 y + 5.21978043650349 xy + 8503.57946593765 y^2 −74.2065948501789 xy^2 −89989.2114133273 y^3 + 339.617068379317 xy^3 + 371678.160794590 y^4 −372.942840325184 xy^4 −446266.728859619 y^5
Inherent shear surface (Fig. 18b) $F(x,y) =$	−0.422720945299102 + 0.521840469958453 x + 3.93657539047443 y
(Shear + In-plane bending) surface (Fig. 20a, green) $F(x,y) =$	3.566536412 + 2.351062084 x − 8.520951175 y − 0.098624011 x^2 + 3.89291132 xy + 0.002650343 x^3 − 0.271337043 x^2y − 1.52909×10^{-5} x^4 + 0.002914693 x^3y
The shear surface of the machine system (Fig. 20a, gold) $F(x,y) =$	−0.286654599109757 + 0.3655246 60088591 x + 2.76844386811610 y − 0.00262834751845358 x^2 − 0.0208634342480003 xy + $1.79462149482027\times10^{-5}$ x^3 + 0.000143337612399050 x^2y
In-plane bending surface of the machine system (Fig. 20b) $F(x,y)$ =	3.27988181337396 + 2.71658674416979 x − 5.75250730666252 y − 0.101252358361013 x^2 + 3.87204788566312 xy + 0.00266828925616349 x^3 − 0.271193705115378 x^2y − $1.52908523478373\times10^{-5}$ x^4 + 0.00291469253373595 x^3y
In-plane bending surface of the inherent system (Fig. 21) $F(x,y)$ =	5.31334366347962 + 3.34900518047926 x − 15.8395034187052 y − 0.120739964621193 x^2 + 6.96493204760085 xy + 0.00339515896379840 x^3 − 0.471212658128505 x^2y − $1.40848344908908\times10^{-5}$ x^4 + 0.00483770942404927 x^3y

Supplementary Information The online version contains supplementary material available at https://doi.org/10.1007/s12289-026-01978-z.

Acknowledgements The authors wish to thank the National Manufacturing Institute Scotland (NMIS) for funding this project and the industrial sponsor Johns Manville (USA) for co-funding, supplying the fabrics used in the study, and sharing expert advice and knowledge.

Author contributions K. D. H. N. Kahavita performed the experiments, analysed the data, and prepared the initial manuscript draft. Co-authors P. Harrison, E. D. McCarthy, M. Zhang and C. M. Ó Brádaigh provided technical guidance, contributed to the interpretation of results, and critically revised the manuscript for important intellectual content. All authors reviewed and approved the final manuscript and agree to be accountable for all aspects of the work.

Data availability No datasets were generated or analysed during the current study.

Declarations

Competing interests The authors declare no competing interests.

Conflict of interest The authors declare that they have no conflict of interest.

Ethical statement The submission contains original research work and has been approved by all authors. The work presented in the manuscript has not been published previously.

References

1. Loos M (2015) Chapter 2 - Composites. Carbon Nanotube Reinforced Composites. William Andrew Publishing, pp 37–72. https://doi.org/10.1016/C2012-0-06123-6
2. Callister W, Rethwisch D (2000) Fundamentals of materials science and engineering. Wiley, London
3. Schrank V, Beer M, Beckers M, Gries T (2017) Polymer-optical fibre (POF) integration into textile fabric structures. Polymer optical fibres. Woodhead Publishing, pp 337–348. https://doi.org/10.1016/B978-0-08-100039-7.00010-5
4. Abdullah SS, Iannucci L, Greenhalgh ES, Abdullah NA (2022) The delamination behaviour of Vectran/Epoxy composites having a novel non-crimp fabric architecture. Compos Part B Eng 228:109413. https://doi.org/10.1016/j.compositesb.2021.109413
5. Bozkurt E, Kaya E, Tanoğlu M (2007) Mechanical and thermal behavior of non-crimp glass fiber reinforced layered clay/epoxy nanocomposites. Compos Sci Technol 67:15–16. https://doi.org/10.1016/j.compscitech.2007.03.021
6. Chen S, Joesbury AM, Yu F, Harper LT, Warrior NA (2022) Optimisation of intra-ply stitch removal for improved formability of biaxial non-crimp fabrics. Compos Part B Eng 229:109464. https://doi.org/10.1016/j.compositesb.2021.109464
7. Colin D, Bel S, Hans T, Hartmann M, Drechsler K (2020) Virtual description of non-crimp fabrics at the scale of filaments including orientation variability in the fibrous layers. Appl Compos Mater 27(4):337–355. https://doi.org/10.1007/s10443-020-09819-1
8. Krieger H, Gries T, Stapleton SE (2018) Shear and drape behavior of non-crimp fabrics based on stitching geometry. IntJ Mater Form 11(5):593–605. https://doi.org/10.1007/s12289-017-1368-1
9. Chen S, McGregor OPL, Harper LT, Endruwei A, Warrior NA (2016) Defect formation during preforming of a bi-axial non-crimp fabric with a pillar stitch pattern. Compos Part A: Appl Sci Manufac 91:156–167. https://doi.org/10.1016/j.compositesa.2016.09.016
10. Bardl G, Nocke A, Hübner M, Pooch M, Schulze M, Heuer H, Schiller M, Kupke R, Klein M (2018) Analysis of the 3D draping behavior of carbon fiber non-crimp fabrics with eddy current technique. Compos Part B: Eng 132:49–60. https://doi.org/10.1016/j.compositesb.2017.08.007
11. Krogh C, Kepler JA, Jakobsen J (2021) Pure and simple: investigating the in-plane shear kinematics of a quasi-unidirectional glass fiber non-crimp fabric using the bias-extension test. IntJ Mater Form 14(6):1483–1495. https://doi.org/10.1007/s12289-021-01642-8
12. Schirmaier FJ, Weidenmann KA, Kärger L, Henning F (2016) Characterisation of the draping behaviour of unidirectional non-crimp fabrics (UD-NCF). Compos Part A Appl Sci Manuf. https://doi.org/10.1016/j.compositesa.2015.10.004
13. Ghazimoradi M, Trejo EA, Carvelli V, Butcher C, Montesano J (2021) Deformation characteristics and formability of a tricot-stitched carbon fiber unidirectional non-crimp fabric. Compos Part A Appl Sci Manuf 145:106366. https://doi.org/10.1016/j.compositesa.2021.106366
14. Härtel F, Harrison P (2014) Evaluation of normalisation methods for uniaxial bias extension tests on engineering fabrics. Compos Part A Appl Sci Manuf. https://doi.org/10.1016/j.compositesa.2014.08.011
15. Kahavita KDHN, McCarthy ED, Zhang M, Ó Brádaigh CM, Harrison P (2023) Characterising the shear resistance of a unidirectional non-crimp glass fabric using modified picture frame and uniaxial bias extension test methods. Int J Mater Form. https://doi.org/10.1007/s12289-023-01765-0
16. Senner T, Kreissl S, Merklein M, Meinhardt J, Lipp A (2014) A modular modeling approach for describing the in-plane forming behavior of unidirectional non-crimp-fabrics. Prod Eng 8:635–643. https://doi.org/10.1007/s11740-014-0561-z
17. Bhat S, Dittel G, Knobel A, Gries T (2022) Investigation of the drapability of elastic-adapted textile reinforcements for double-curved concrete panels, in *SAMPE EUROPE Conference and Exhibition 2022*, Hamburg. https://www.nasampe.org/store/viewproduct.aspx?id=23969913
18. Tong L, Mouritz AP, Bannister MK (2002) 3D fibre reinforced polymer composites. Elsevier. https://doi.org/10.1016/B978-0-08-043938-9.X5012-1
19. Schirmaier FJ, Dörr D, Henning F, Kärger L (2017) A macroscopic approach to simulate the forming behaviour of stitched unidirectional non-crimp fabrics (UD-NCF). Compos A 102:322–335. https://doi.org/10.1016/j.compositesa.2017.08.009
20. Ghazimoradi M, Trejo EA, Butcher C, Montesano J (2022) Characterizing the macroscopic response and local deformation

mechanisms of a unidirectional non-crimp fabric. Compos Part A Appl Sci Manuf 156:106857. https://doi.org/10.1016/j.compositesa.2022.106857
21. Schäfer B, Zheng R, Naouar N, Kärger L (2023) Membrane behavior of uni- and bidirectional non-crimp fabrics in off-axis-tension tests. Int J Mater Form 16(6):68. https://doi.org/10.1007/s12289-023-01792-x
22. Spencer AJM, Soldatos KP (2007) Finite deformations of fibre-reinforced elastic solids with fibre bending stiffness. Int J Non-Linear Mech 42(2):355–368. https://doi.org/10.1016/j.ijnonlinmec.2007.02.015
23. Cuomo M, dell'Isola F, Greco L, Rizzi NL (2017) First versus second gradient energies for planar sheets with two families of inextensible fibres: investigation on deformation boundary layers, discontinuities and geometrical instabilities. Compos Part B Eng 115:423–448. https://doi.org/10.1016/j.compositesb.2016.08.043
24. Bai R, Guzman-Maldonado E, Zheng R, Colmars J (2024) Influence of in-plane bending behaviour on textile composite reinforcement forming. Int J Mech Sci 273:109206. https://doi.org/10.1016/j.ijmecsci.2024.109206
25. McGuinness GB, ÓBrádaigh CM (1998) Characterisation of thermoplastic composite melts in rhombus-shear: the picture-frame experiment. Compos Part A Appl Sci Manuf 29:115–132. https://doi.org/10.1016/S1359-835X(97)00061-4
26. Barbagallo G, Madeo A, Azehaf I, Giorgio I, Morestin F, Boisse P (2017) Bias extension test on an unbalanced woven composite reinforcement: experiments and modeling via a second-gradient continuum approach. J Compos Mater 51(2):153–170. https://doi.org/10.1177/0021998316643577
27. Harrison P, Camacho LFG (2021) Deep draw induced wrinkling of engineering fabrics. Int J Solids Struct 212:220–236. https://doi.org/10.1016/j.ijsolstr.2020.12.003
28. Harrison P, Alvarez MF, Anderson D (2018) Towards comprehensive characterisation and modelling of the forming and wrinkling mechanics of engineering fabrics. Int J Solids Struct 154:2–18. https://doi.org/10.1016/j.ijsolstr.2016.11.008
29. Viisainen J (2022) Wrinkling behaviour of biaxial non-crimp fabrics during preforming. University of Cambridge, Cambridge. https://doi.org/10.17863/CAM.81052
30. Rueden C, Dietz C, Horn M, Schindelin J, Northan B, Berthold M, Eliceiri K ImageJ Ops [Software], 2016. [Online]. Available: https://imagej.net/Ops
31. Alsayednoor F, Lennard F, Yu WR, Harrison P (2017) Influence of specimen pre-shear and wrinkling on the accuracy of uniaxial bias extension test results. Compos Part A Appl Sci Manuf 101:81–97. https://doi.org/10.1016/j.compositesa.2017.06.006
32. Kahavitage HNK, Dona (2025) Experimental characterisation and forming analysis of pure unidirectional stitched glass fibre non-crimp fabric (Doctoral dissertation), University of Glasgow, Glasgow. https://theses.gla.ac.uk/id/eprint/85018
33. Harrison P (2016) Modelling the forming mechanics of engineering fabrics using a mutually constrained pantographic beam and membrane mesh. Composite: Part A 81:145–157. https://doi.org/10.1016/j.compositesa.2015.11.005
34. Harrison P, Wiggers J, Long A (2008) Normalisation of shear test data for rate-independent compressible fabrics. J Compos Mater 42:2315–2344. https://doi.org/10.1063/1.2729646
35. Pourtier J, Duchamp B, Kowalski M, Wang P, Legrand X, Soulat D (2019) Two-way approach for deformation analysis of non-crimp fabrics in uniaxial bias extension tests based on pure and simple shear assumption. Int J Mater Form 12(6):995–1008. https://doi.org/10.1007/s12289-019-01481-8
36. Kahavita N, Harrison P Protocols.io, 02 July 2024. [Online]. Available: https://doi.org/10.17504/protocols.io.81wgbyy93vpk/v1
37. Harrison P, Taylor E, Alsayednoor J (2018) Improving the accuracy of the uniaxial bias extension test on engineering fabrics using a simple wrinkle mitigation technique. Composites Part A 108:53–61. https://doi.org/10.1016/j.compositesa.2018.02.025
38. Willems A, Lomov SV, Verpoest I, Vandepitte D (2008) Optical strain fields in shear and tensile testing of textile reinforcements. Compos Sci Technol 68:807–819. https://doi.org/10.1016/j.compscitech.2007.08.018
39. Krogh C, White KD, Sabato A, Sherwood JA (2020) Picture-frame testing of woven prepreg fabric: an investigation of sample geometry and shear angle acquisition. Int J Mater Form 13:341–353. https://doi.org/10.1007/s12289-019-01499-y
40. Harrison P, Abdiwi F, Guo Z, Potluri P, Yu W (2012) Characterising the shear–tension coupling and wrinkling behaviour of woven engineering fabrics. Compos Part A: Appl Sci Manufac 43:903–914. https://doi.org/10.1016/j.compositesa.2012.01.024